MODELING AND NUMERICAL ANALYSIS OF THE CHOLESTERIC LANDAU-DE GENNES MODEL

A Dissertation

Submitted to the Graduate Faculty of the
Louisiana State University and
Agricultural and Mechanical College
in partial fulfillment of the
requirements for the degree of
Doctor of Philosophy

in

The Department of Mathematics

by
Andrew L. Hicks
B.A., Ave Maria University, 2017
M.S., Louisiana State University, 2020
May 2024

Acknowledgments

First, I would like to thank my parents for their love, support, and advice for me during all of my years of education. I couldn't have done this without them.

Next, I would like to thank Mr. Chris Tuttle, my elementary school teacher who first helped me realize that mathematics is an enjoyable subject worth excelling in. I would also like to acknowledge Fr. Travis Abadie, another teacher who continued to fuel my mathematical curiosity during high school.

I also extend my thanks to Dr. Michael Marsalli, whose guidance during my undergraduate at Ave Maria University was invaluable. I want to thank Dr. Justin Lynd as well, who undoubtedly helped mature me greatly as a mathematician.

As for those at LSU who helped me in my journey, there are plenty of names I could give. I would first like to acknowledge my advisor Prof. Shawn Walker for his guidance and input in the writing of this dissertation, for advising me, and for developing my skills in numerical analysis. I also want to thank Prof. Stephen Shipman for his help and advice in many ways throughout the years, and for always being someone I could talk to about a wide variety of topics. In a special way I thank Prof. James Oxley for being an incredibly generous mentor to all his students, and for helping me develop as a teacher of mathematics over the years and guiding me in writing an effective teaching statement. Last but not least are the friends I made along the way in the mathematics department: Iswarya, Miao, Jinpu, SeongHee, Arun, Jorge, Jeremy, Yongho, Doosung, Hongki, and many others. Thank you all for making these past six years some of the best in my life.

Table of Contents

Abstract

This thesis gives an analysis of modeling and numerical issues in the Landau-de Gennes (LdG) model of nematic liquid crystals (LCs) with cholesteric effects. We derive various time-step restrictions for a (weighted) L^2 gradient flow scheme to be energy decreasing. Furthermore, we prove a mesh size restriction, for finite element discretizations, that is critical to avoid spurious numerical artifacts in discrete minimizers that is not well-known in the LC literature, particularly when simulating cholesteric LCs that exhibit "twist".

Furthermore, we perform a computational exploration of the model and present several numerical simulations in 3-D, on both slab geometries and spherical shells, using a fully-implicit gradient flow scheme applied to a finite element discretization of the model. The simulations are consistent with experiments, illustrate the richness of the cholesteric model, and demonstrate the importance of the mesh size restriction.

Chapter 1. Introduction

New types of materials are a necessary component in many new technologies [49, 75]. Liquid crystals (LCs), in particular, are finding innovative uses in many material design problems. Originally, nematic LCs were developed and commercialized for their optical properties [31, 17, 47, 86, 53, 29], which is what enables LC displays. A key component of the functionality of LC displays is the mechanical response of LCs to electric and magnetic actuation [24, 5, 82]. Indeed, LCs' mechanical actuation enables various applications, such as liquid crystal elastomers [102, 32, 15, 79], dynamic shape control of elastic bodies [25, 95], and self-assembly of colloids [82, 89, 90].

Many nematic LCs are characterized by several material constants [68, 70], which provide useful tuning parameters that can be tailored to specific applications. This thesis is concerned with the modeling and numerical simulation of a particular sub-type of LC which are known as cholesteric nematic LCs where the molecules have a chiral structure that affects their actuation and equilibrium behavior [31, 88, 60]. Cholesteric LCs are present in many biological systems, such as viruses [37], chitin [74], and the structured coloring of the scarab beetle [4]. These materials often exhibit stripe patterns in their optical response, which can be exploited for engineering materials for the built environment [59, 81]. This thesis presents a numerical method and analysis for simulating cholesteric LCs in order to predict their structural features. Numerical modeling can yield greater insight into the functional effects of cholesteric LCs in biological systems and enable the design of programmable materials [66, 44, 58].

Numerical analysis and simulation of LCs began with an earlier model known as the Oseen-Frank model, which uses a vector field as the order parameter, e.g. see [7, 13,

76, 1, 2, 3, 33, 72, 73, 93, 69, 35] and [27, 46, 54, 98, 99, 94] which model full dynamics. The multi-constant Oseen-Frank model was the workhorse of the LCD industry. However, non-orientable line fields cannot be modeled with Oseen-Frank [19] and defects (see Remark 1) require regularization. This is why the LdG model is usually preferred because it can model general line fields with defects. Many numerical methods and implementations exist for the standard LdG model, e.g. [42, 8, 30, 14, 18, 61, 100, 101]. These methods have also been extended to tackle cholesteric LCs [78, 89, 88, 60]. However, to the best of our knowledge, a proper numerical analysis of the general LdG model that includes the cholesteric term appears to be lacking.

1.1. Summary

This thesis gives a full numerical analysis of the general Landau-de Gennes model with cholesteric effects. We address both computing L^2 gradient flow dynamics, as well as solving the equilibrium equations that characterize a local minimizer. In particular, restrictions on the time-step and mesh-size appear that are not obvious to most liquid crystal scientists. For example, the well-known convex-splitting scheme for handling the bulk potential has a time-step restriction depending on the cholesteric twist. Moreover, if the computational mesh size is not small enough, unphysical solutions may occur (i.e. the computed local minimizer may exhibit numerical artifacts). Furthermore, we investigate two slightly different cholesteric models which can potentially produce very different results. We also demonstrate that the choice of initial condition can significantly affect which local minimizer is found, as well as the speed of convergence to a solution.

Part of the contribution of this thesis is to present these issues, and how to han-

dle them, to a diverse audience of computational scientists. Another contribution is to explore the cholesteric LdG model and illustrate the rich phenomena that result from it; see [81, 60, 88] for related work. Our presentation here should enable more robust computations for exploring the LC physics and device design of systems that are governed by the cholesteric Landau-de Gennes model.

1.2. Notational Conventions

We focus on three dimensional liquid crystal models, thus 2-tensors are elements of $\mathbb{R}^{3\times 3}$ denoted by standard capital letters, e.g. the 3×3 identity tensor is written as I. Moreover, 4-tensors are elements of $\mathbb{R}^{3^4}$ and denoted by calligraphic capitals. Constants and scalar-valued functions will be denoted by lowercase letters. Moreover, Greek letters will typically denote certain important functions and constants. Vectors will be denoted by boldface lowercase letters.

Let the D operator denote differentiation of a scalar-valued function with respect to each argument of a tensor; that is, for any function ϕ mapping to $\mathbb{R}$, define

$$D\phi(P) := \left[\frac{\partial \phi}{\partial P_{ij}}\right]_{i,j=1}^{3}, \tag{1.1}$$

for all $P \in \mathbb{R}^{3\times 3}$. Likewise, let the D^2 operator denote the Hessian; that is, for all ϕ as above define

$$D^2\phi(P) := \left[\frac{\partial^2 \phi}{\partial P_{ij}\partial P_{kl}}\right]_{i,j,k,l=1}^{3}, \tag{1.2}$$

for all $P \in \mathbb{R}^{3\times 3}$. For derivatives with respect to spatial coordinates, we use $\partial_i \phi := \partial_{x_i}\phi$, where $\mathbf{x} = (x_1, x_2, x_3)^\dagger$ is the spatial coordinate, or we use the comma-subscript notation, e.g. $\phi_{,i} := \partial_i \phi$ and $P_{ij,k} := \partial_k P_{ij}$.

Next, we define the L^2 inner products on Ω and Γ:

$$(A,B)_\Omega := \int_\Omega A : B \, d\mathbf{x}, \qquad (A,B)_\Gamma := \int_\Gamma A : B \, dS(\mathbf{x}),$$

where A, B are tensors and : is the Frobenius inner-product (similar relations hold for vectors and scalars). Moreover, $|A| = \sqrt{A : A}$ is the Frobenius norm. The norms for $L^2(\Omega)$ and $H^1(\Omega)$ are then given by

$$\|P\|_{0,\Omega}^2 := (P,P)_\Omega \,, \qquad \|P\|_{0,\Gamma}^2 := (P,P)_\Gamma \,,$$

$$\|P\|_{1,\Omega}^2 := (P,P)_\Omega + (\nabla P, \nabla P)_\Omega \,, \qquad |P|_{1,\Omega}^2 := (\nabla P, \nabla P)_\Omega \,,$$

where $\nabla P = [\partial_k P_{ij}]_{i,j,k=1}^3$ is the gradient of P and $|P|_{1,\Omega}$ is the $H^1(\Omega)$ *semi*-norm. Similarly for the $H^2(\Omega)$ norm and semi-norm we have

$$\|P\|_{2,\Omega}^2 := (P,P)_\Omega + (\nabla P, \nabla P)_\Omega + \left(\nabla^2 P, \nabla^2 P\right)_\Omega \,, \qquad |P|_{2,\Omega}^2 := \left(\nabla^2 P, \nabla^2 P\right)_\Omega \,,$$

where $\nabla^2 P = [\partial_l \partial_k P_{ij}]_{i,j,k,l=1}^3$ denotes the Hessian of the tensor P. When we need to specify an $L^p(\Omega)$ or $L^p(\Gamma)$ norm for $1 \le p < \infty$ and $p \ne 2$, we use

$$\|P\|_{0,p,\Omega}^p := (|P|^p, 1)_\Omega \,, \qquad \|P\|_{0,p,\Gamma}^p := (|P|^p, 1)_\Gamma \,.$$

And finally, for the $L^\infty(\Omega)$ norm we use

$$\|P\|_{0,\infty,\Omega} := \operatorname*{ess\,sup}_\Omega |P|, \qquad \|P\|_{0,\infty,\Gamma} := \operatorname*{ess\,sup}_\Gamma |P|.$$

Chapter 2. Liquid Crystal Theory

We briefly review the Landau-de Gennes theory for a nematic LC phase.

2.1. Coarse-grained Molecular Theory

LCs are a *meso-phase* of matter where the ordered macroscopic state is between a spatially disordered liquid and a fully crystalline solid [91]. Nematic LC molecules are rod-like and are free to slide about, meaning no positional order is maintained. The (partial) spatial order that is maintained is *orientational*, i.e. the rod-like molecules prefer to be aligned with their neighbors due to molecular forces. When long ranged orientational order exists, it is known as the *nematic phase*. Since the LC molecules have fore-aft symmetry, their orientational order throughout space is modeled by a line field (as opposed to a vector field). The Landau-de Gennes (LdG) theory [31, 91, 84] introduces a *tensor-valued* function Q to describe the local order (at each point in space) in the LC material. In particular, the eigenframe of Q yields information about the statistics of the distribution of LC molecule orientations (see Section 2.1). Equilibrium configurations of an LC material are modeled by finding a function Q that minimizes an appropriate energy functional that includes a non-convex bulk potential, an "elastic" contribution involving spatial derivatives of Q, as well as a "surface anchoring" energy (see Section 2.2).

We derive the Q-tensor order parameter of the LdG model following the presentation in [91]. Let Ω be a domain containing liquid crystals, and consider a small region around a point $\mathbf{x} \in \Omega$. It is essentially intractable to model the individual LC molecules at every point in space. Thus, we adopt a coarse-grained approach and introduce a probability distribution $f(\mathbf{r})$ which specifies the probability density of finding an LC molecule

oriented in the direction of $\mathbf{r} \in S^2$ at $\mathbf{x}$, where S^2 is the unit sphere. We also give f the property that $f(-\mathbf{r}) = f(\mathbf{r})$, since LC molecules are practically indistinguishable under a mirror reflection.

The fundamental quantity that captures the basic statistical distribution of the LC molecules is the covariance 2-tensor M given by

$$M := \int_{S^2} (\mathbf{r} \otimes \mathbf{r}) f(\mathbf{r})\, dA. \tag{2.1}$$

The properties of M to note are that $\mathrm{tr}M = 1$, $M^\dagger = M$, and $\mathbf{n}^\dagger M \mathbf{n} = \langle \cos^2\theta \rangle$ for any fixed $\mathbf{n} \in S^2$, where $\mathbf{n} \cdot \mathbf{r} = \cos\theta$ and $\langle \cdot \rangle$ indicates the statistical average. A constant f (representing "isotropic," i.e. randomly oriented molecules) yields $M = \frac{1}{3} I$, which we will denote by M_0. The Q-tensor is obtained by simply normalizing M using M_0: $Q := M - M_0$. Thus, in addition to Q being symmetric, it is also traceless and vanishes when f is isotropic, i.e. for every point $\mathbf{x} \in \Omega$, $Q(\mathbf{x})$ belongs to

$$\mathbf{S}_0 := \{Q \in \mathbb{R}^{3\times 3} \mid Q^\dagger = Q,\ \mathrm{tr}(Q) = 0\}. \tag{2.2}$$

Next, writing Q in its eigenframe, we have

$$Q = \lambda_i \mathbf{e}_i \otimes \mathbf{e}_i, \tag{2.3}$$

where $\lambda_i \equiv \lambda_i(Q)$ are the eigenvalues of Q, and $\mathbf{e}_i$ are the normalized eigenvectors. From the probability density and definition of Q, one can show that each λ_i satisfies

$$-\frac{1}{3} \leq \lambda_i(Q) \leq \frac{2}{3}, \quad \text{for } i = 1, 2, 3. \tag{2.4}$$

Also, since Q is traceless, (2.3) implies that $\lambda_3 = -(\lambda_1 + \lambda_2)$. In the case that all eigenvalues are equal, they are 0 and we simply have $Q = 0$, the isotropic state. Likewise, when

all eigenvalues are different from one another, we have what is called the biaxial state. Most commonly, when just two of the eigenvalues are equal, we have the so-called *uniaxial* state, where Q may be expressed as

$$Q = s\left(\mathbf{n}\otimes\mathbf{n} - \frac{1}{3}I\right), \tag{2.5}$$

where s is called the *degree-of-orientation*, and is a measure of the orientational order of the LC molecules at each point, and $\mathbf{n}$ is called the *director*, which has unit length, $|\mathbf{n}| = 1$, and represents the average direction in which the molecules are pointing. If $\cos\theta = \mathbf{r}\cdot\mathbf{n}$ as above, then

$$s = \frac{3\langle\cos^2\theta\rangle - 1}{2}, \tag{2.6}$$

which implies that $-\frac{1}{2} \leq s \leq 1$. For many nematic LCs, the default state is usually uniaxial with a particular value of s that depends on the material. Typically, the optimal s is in the range $0.5 \leq s \leq 0.8$ [31].

Remark 1. *Defects are ubiquitous in liquid crystals. They correspond to sudden spatial changes in Q with particular characteristics. Specifically, when Q is uniaxial, the director $\mathbf{n}$ has a discontinuity which is regularized by s vanishing at the point of discontinuity. The degree of the defect is the "winding number" of the director; see [87, Sec. 7] for a short discussion, as well as [63] for a more extensive introduction to the mathematical aspects of defects in liquid crystals.*

2.2. Landau-de Gennes Theory

Next, we model the state of an LC system through a tensor-valued function $Q : \Omega \to \mathbf{S}_0$, where Ω is the physical domain of interest. We assume throughout that Ω has Lipschitz boundary Γ with outward pointing unit normal vector $\boldsymbol{\nu}$ (e.g. box-like domains

and domains with smooth boundary are allowed). The free energy of the LdG model is defined as [68, 70, 78]:

$$\begin{aligned}\mathcal{E}[Q] := &\int_\Omega f(Q, \nabla Q)\, d\mathbf{x} + \int_\Omega \psi(Q)\, d\mathbf{x} \\ &+ \int_\Gamma g(Q)\, dS(\mathbf{x}) + \int_\Gamma \phi(Q)\, dS(\mathbf{x}) - \int_\Omega \chi(Q)\, d\mathbf{x},\end{aligned} \tag{2.7}$$

with the elastic energy (with twist component as in [88, 78]) given by

$$\begin{aligned}f(Q, \nabla Q) := \frac{1}{2}\Big(&\ell_1 |\nabla Q|^2 + \ell_2 |\nabla \cdot Q|^2 + \ell_3 (\nabla Q)^\dagger \vdots \nabla Q \\ &+ 4\ell_1 \tau_0 \nabla Q \vdots (\varepsilon \cdot Q)\Big),\end{aligned} \tag{2.8}$$

where $\{\ell_i\}_{i=1}^3$ (units of $\mathrm{J} \cdot \mathrm{m}^{-1}$) and τ_0 (units of m^{-1}) are material dependent elastic constants, and

$$\begin{aligned}|\nabla Q|^2 := Q_{ij,k} Q_{ij,k}, \quad |\nabla \cdot Q|^2 := Q_{ij,j} Q_{ik,k}, \\ (\nabla Q)^\dagger \vdots \nabla Q := Q_{ij,k} Q_{ik,j}, \quad \nabla Q \vdots (\varepsilon \cdot Q) := \varepsilon_{jkl} Q_{ik,l} Q_{ij},\end{aligned} \tag{2.9}$$

where we use the convention of summation over repeated indices and ε_{jkl} is the Levi-Civita tensor. The transpose in the third term indicates to swap one of the Q indices with the derivative index. The elastic constants in the LdG model can be related to the elastic constants in the Oseen-Frank model (see [68, 70]). Note that taking $\ell_i = 0$, for $i = 2, 3$, and $\tau_0 = 0$ gives the often used one constant LdG model. More complicated models can also be considered [70, 31, 84].

Next, the bulk potential ψ is a double-well type of function that is given by

$$\psi(Q) = a_0 - \frac{a_2}{2}\mathrm{tr}(Q^2) - \frac{a_3}{3}\mathrm{tr}(Q^3) + \frac{a_4}{4}\big(\mathrm{tr}(Q^2)\big)^2. \tag{2.10}$$

Above, a_2, a_3, a_4 are material parameters (units of $\mathrm{J} \cdot \mathrm{m}^{-3}$) such that a_2, a_3, a_4 are positive; a_0 is a convenient constant to ensure $\psi \geq 0$. Stationary points of ψ are either uni-

axial or isotropic Q-tensors [65]. Combined with (2.5), the critical values of the scalar order parameter s for $\psi(Q(s))$, where $Q(s)$ is uniaxial, are $s = 0$ (local maximum), $s = \left(a_3 - \sqrt{a_3^2 + 24a_2a_4}\right)/4a_4$ (local minimum) and the global minimum [84]:

$$s_0 = \frac{a_3 + \sqrt{a_3^2 + 24a_2a_4}}{4a_4}, \tag{2.11}$$

and is typically in the range $0.5 \leq s_0 \leq 0.8$ [31] for a_2 sufficiently large positive, which we shall always assume. Note that, for thermotropic LCs, a_2 is temperature dependent where a_2 can become a large negative parameter for high enough temperature [70, 91]. In this case, ψ becomes a convex function with a global minimum at $Q = 0$ (the isotropic state). Though this potential is rather simplistic in that it does not guarantee that the eigenvalues of Q remain in the physical range (2.4), it is effective in most modeling situations (c.f. [65]).

The surface energy, composed of the quadratic $g(Q)$ and higher-order $\phi(Q)$, accounts for *weak anchoring* of the LC (i.e. penalization of boundary conditions). For example, a Rapini-Papoular type anchoring energy [12] can be considered:

$$g(Q) = \frac{w_0}{2}|Q - Q_\Gamma|^2 + \frac{w_1}{2}|\tilde{Q} - \tilde{Q}^\perp|^2, \quad \phi(Q) = \frac{w_2}{4}(|\tilde{Q}|^2 - s_0^2)^2, \tag{2.12}$$

where w_0, w_1, and w_2 are positive constants (units of $\mathrm{J} \cdot \mathrm{m}^{-2}$), $Q_\Gamma(x) \in \mathbf{S}_0$ for all $\mathbf{x} \in \Gamma$, and s_0 is the scalar order parameter of the uniaxial Q that minimizes the double well. We set $\tilde{Q} := Q + \frac{s_0}{3}I$, and define the standard projection onto the plane orthogonal to $\boldsymbol{\nu}$, that is, $Q^\perp := \Pi Q \Pi$ where $\Pi = I - \boldsymbol{\nu} \otimes \boldsymbol{\nu}$. We define Q_Γ to be uniaxial of the form

$$Q_\Gamma = s_0 \left(\boldsymbol{\nu} \otimes \boldsymbol{\nu} - \frac{1}{3}I\right). \tag{2.13}$$

Figure 2.1. Left: Illustration of homeotropic anchoring. Here the director $\mathbf{n}$, which we denote by $\mathbf{n}_\parallel$, is closely aligned with the outward normal vector $\boldsymbol{\nu}$; the closesness of alignment is controlled by the constant w_0. Right: Illustration of planar degenerate anchoring. Here the director $\mathbf{n}$, which we denote by $\mathbf{n}_\perp$, is closely aligned tangent to the surface; the closesness of alignment is controlled by the constants w_1 and w_2.

The w_0 term in (2.12) models homeotropic (normal) anchoring, while w_1 and w_2 model planar degenerate anchoring. See Figure 2.1 for an illustration.

The function $\chi(\cdot)$ accounts for interactions with external fields. For example, the energy density of a dielectric LC with fixed boundary potential is given by $-1/2\,\mathbf{D}\cdot\mathbf{E}$ [92], where the electric displacement $\mathbf{D}$ is related to the electric field $\mathbf{E}$ by the linear constitutive law [40, 31, 16]:

$$\mathbf{D} = \boldsymbol{\varepsilon}\mathbf{E} = \bar{\varepsilon}\mathbf{E} + \varepsilon_{\mathrm{a}} Q\mathbf{E}, \quad \boldsymbol{\varepsilon}(Q) = \bar{\varepsilon} I + \varepsilon_{\mathrm{a}} Q, \tag{2.14}$$

where $\boldsymbol{\varepsilon}$ is the LC material's dielectric tensor and $\bar{\varepsilon}$, ε_{a} are constitutive dielectric permittivities. Thus, we may rewrite the dielectric energy density as

$$-\frac{1}{2}\mathbf{D}\cdot\mathbf{E} = -\frac{1}{2}\bar{\varepsilon}|\mathbf{E}|^2 + \chi(Q), \quad \chi(Q) = -\frac{1}{2}\varepsilon_{\mathrm{a}}\mathbf{E}\cdot Q\mathbf{E} \equiv -\frac{1}{2}\varepsilon_{\mathrm{a}}\mathbf{E}\otimes\mathbf{E} : Q, \tag{2.15}$$

where $\chi(Q)$ has units of $\mathrm{J/m^3}$. Note that we do not include the term $(\bar{\varepsilon}/2)|\mathbf{E}|^2$ in (2.7) because it is independent of Q.

2.3. Non-dimensionalization

We start by noting that Q and s are already non-dimensional. Lengths and coordinates are non-dimensionalized by introducing a characteristic length ξ, e.g. $\hat{\mathbf{x}} = \mathbf{x}/\xi$, where $\hat{\mathbf{x}}$ is non-dimensional. Then, set ℓ_{m} to be the maximum or average of $\{|\ell_i|\}_{i=1}^3$ and simply divide (2.7) by $\ell_{\mathrm{m}}\cdot\xi$ to obtain a dimensionless energy. This effectively rescales

all spatial derivatives, integral measures, and the various constants in the problem. Other non-dimensionalizations are possible (c.f. [39, Sec. 2.]).

However, $\psi(Q)$ and $\phi(Q)$ are non-convex functions, which significantly affect the numerical analysis of the model. Thus, we describe their non-dimensionalization in more detail. Set $c_0 := \psi(0) - \psi(Q(s_0))$ and define the non-dimensional bulk potential by $\widehat{\psi}(Q) := \psi(Q)/c_0$; thus, $\widehat{\psi}(0) - \widehat{\psi}(Q(s_0)) = 1$. This immediately implies that $|D\widehat{\psi}(Q)| = O(1)$ as Q varies between the isotropic state and the global minimum of $\widehat{\psi}$. Then, upon introducing the non-dimensional parameter $\eta := \sqrt{\ell_{\mathrm{m}}/(c_0\xi^2)}$, we have

$$\frac{1}{\ell_{\mathrm{m}}\xi}\int_{\Omega}\psi(Q)\,d\mathbf{x} = \frac{1}{\eta^2}\int_{\widehat{\Omega}}\widehat{\psi}(Q)\,d\hat{\mathbf{x}}, \tag{2.16}$$

where $\widehat{\Omega}$ is the scaled domain. As for $\phi(Q)$, upon setting $\widehat{\phi}(Q) = \left(|\tilde{Q}|^2 - s_0^2\right)^2/4$ and $\omega := \ell_{\mathrm{m}}/(w_2\xi)$, we have

$$\frac{1}{\ell_{\mathrm{m}}\xi}\int_{\Gamma}\phi(Q)\,dS(\mathbf{x}) = \frac{1}{\omega}\int_{\widehat{\Gamma}}\widehat{\phi}(Q)\,d\hat{S}(\hat{\mathbf{x}}), \tag{2.17}$$

where $\widehat{\Gamma}$ is the scaled boundary. Then, the total non-dimensional energy is

$$\begin{aligned}\widehat{\mathcal{E}}[Q] = &\int_{\widehat{\Omega}}\widehat{f}(Q,\widehat{\nabla}Q)\,d\hat{\mathbf{x}} + \frac{1}{\eta^2}\int_{\widehat{\Omega}}\widehat{\psi}(Q)\,d\hat{\mathbf{x}}\\ &+\int_{\widehat{\Gamma}}\widehat{g}(Q)\,d\hat{S}(\hat{\mathbf{x}}) + \frac{1}{\omega}\int_{\widehat{\Gamma}}\widehat{\phi}(Q)\,d\hat{S}(\hat{\mathbf{x}}) - \int_{\widehat{\Omega}}\widehat{\chi}(Q)\,d\hat{\mathbf{x}}.\end{aligned} \tag{2.18}$$

For simplicity, we drop the "hat" notation for the remainder of the thesis.

Remark 2. *The LdG model will not create sharp point (line) discontinuities in two (three) dimensions because $Q(t,\cdot) \in H^1(\Omega;\mathbf{S}_0)$ (see Section 3.1). For example, $\mathbf{n} = \mathbf{x}/|\mathbf{x}|$ is a unit length director with a point defect at the origin, but $\mathbf{n} \notin H^1(\Omega;\mathbb{R}^2)$; thus, the corresponding uniaxial Q, via (2.5), is not in $H^1(\Omega;\mathbf{S}_0)$.*

Therefore, any potential discontinuities get smoothed out causing Q to vanish there. A physical interpretation of this is that the liquid crystal "melts" in a small region around the defect, i.e. the LC material loses all orientational order. The size of the melt region is controlled by the bulk potential parameter η. Thus, in the LdG model, the location of defects are usually identified with regions where $|Q| = 0$. For more information on defects, see [23, 22, 80, 91, 48, 63, 71, 56, 19].

2.4. The Cholesteric LdG Model

Cholesteric LCs are created by adding a chiral dopant (i.e. molecules with a chiral structure) to nematic LCs. This induces a helical superstructure on the nematic phase, which means the local behavior of the LC is nematic (i.e. line segments are aligned with their immediate neighbors) but the larger, super-molecular arrangement of the line segments follows a helical structure with a certain periodicity (or pitch), p. By varying the amount of dopant, one can tune the periodicity from infinity to about 100 nm [81, Sec. 2.2]. The physical manifestation of the cholesteric phase is that the helix modulates the optical properties in a periodic fashion.

The cholesteric, LdG model in (2.7) can be obtained through a mapping procedure from the cholesteric, Oseen-Frank (director) model (see [68]). But we also consider a slightly different cholesteric model given in [88]. In the following sections, we relate this model (which we refer to as the cholesteric model) to the LdG model we have defined in Section 2.2. The elastic energy in [88] is, mainly, a rewriting of the terms in (2.8). However, there is an implicit interference of the elastic energy in [88] with the bulk potential that brings up a modeling issue we highlight in Section 2.4.2.

2.4.1. Elastic energy

The cholesteric model in [88] gives the elastic energy as

$$f_{\text{grad}}(Q) = \left(\frac{\breve{\ell}_1}{2}\right)|\nabla \times Q + 2\tau_0 Q|^2 + \left(\frac{\breve{\ell}_2}{2}\right)|\nabla \cdot Q|^2 + \left(\frac{\breve{\ell}_{24}}{2}\right)(Q_{ij,k}Q_{ik,j} - Q_{ij,j}Q_{ik,k}), \quad (2.19)$$

where $\breve{\ell}_1$, $\breve{\ell}_2$, $\breve{\ell}_{24}$ are elastic constants, $\tau_0 = 2\pi/p$ with p being the pitch, and

$$\nabla \times Q = \varepsilon_{ikl} Q_{lj,k} \mathbf{e}^i \otimes \mathbf{e}^j, \quad (2.20)$$

where $\mathbf{e}^i$ is the ith vector in the standard basis of $\mathbb{R}^3$. This is referred to as the curl of Q and is consistent with the definition of curl for vectors, which is defined for a vector $\mathbf{v} = (v_1, v_2, v_3)^\dagger$ as $\nabla \times \mathbf{v} = \varepsilon_{ikl}(\partial_k v_l)\mathbf{e}^i$. In fact, the columns of $\nabla \times Q$ are the curls of the corresponding columns of Q. The term $|\nabla \times Q + 2\tau_0 Q|^2$ is what frustrates the equilibrium state from having a constant director and models the chiral structure of the molecules. As we will see in the numerical results, choosing $\tau_0 > 0$ causes a "twisting" of the director throughout the LC domain.

It is a straightforward exercise in index notation to prove the identity $|\nabla \times Q|^2 = Q_{ij,k}Q_{ij,k} - Q_{ij,k}Q_{ik,j}$. Moreover, from the definition of $\nabla \times Q$, we have the identity $(\nabla \times Q) : Q = (\varepsilon_{ikl} Q_{lj,k} \mathbf{e}^i \otimes \mathbf{e}^j) : Q = \varepsilon_{ikl} Q_{lj,k} Q_{ij}$.

With this, we can rewrite (2.19) in the form of (2.8) by first noting that

$$\begin{aligned}\left(\frac{\breve{\ell}_1}{2}\right)|\nabla \times Q + 2\tau_0 Q|^2 = \left(\frac{\breve{\ell}_1}{2}\right)Q_{ij,k}Q_{ij,k} - \left(\frac{\breve{\ell}_1}{2}\right)Q_{ij,k}Q_{ik,j} \\ + \left(\frac{4\breve{\ell}_1}{2}\right)\tau_0 \varepsilon_{ikl} Q_{lj,k} Q_{ij} + 2\breve{\ell}_1 \tau_0^2 |Q|^2.\end{aligned}$$

From here, we note that $\text{tr}(Q^2) \equiv |Q|^2$, rearrange the terms and group them as:

$$\begin{aligned}f_{\text{grad}}(Q) = \left(\frac{\breve{\ell}_1}{2}\right)Q_{ij,k}Q_{ij,k} + \left(\frac{\breve{\ell}_2 - \breve{\ell}_{24}}{2}\right)Q_{ij,j}Q_{ik,k} \\ + \left(\frac{\breve{\ell}_{24} - \breve{\ell}_1}{2}\right)Q_{ij,k}Q_{ik,j} + \left(\frac{4\breve{\ell}_1}{2}\right)\tau_0 \varepsilon_{ikl} Q_{lj,k} Q_{ij} + 2\breve{\ell}_1 \tau_0^2 \text{tr}(Q^2).\end{aligned} \quad (2.21)$$

We then use the frame-indifferent invariants in (2.9) to map these constants to the LdG elastic and twist energy densities as given in (2.8), i.e.

$$\ell_1 = \breve{\ell}_1, \qquad \ell_2 = \breve{\ell}_2 - \breve{\ell}_{24}, \qquad \ell_3 = \breve{\ell}_{24} - \breve{\ell}_1, \tag{2.22}$$

where the twist constant τ_0 is the same in both models. Note that there is an extra term of $|Q|^2 \equiv \mathrm{tr}(Q^2)$ in (2.21) that is not found in (2.8) but does appear in (2.10). We discuss the implications of this in Section 2.4.2.

2.4.2. Alternative Cholesteric Model

In [78], they consider the (cholesteric) elastic energy as not containing a $\mathrm{tr}(Q^2)$ term like [88] does. Indeed, keeping this term can have a significant effect on the behavior of energy minimizers.

For simplicity of exposition, we assume all energies have been non-dimensionalized, take $\ell_1 = 1$, $\tau_0 > 0$, and set the other elastic constants to zero. If we keep the $\mathrm{tr}(Q^2)$ term in (2.21), it will combine with the a_2 coefficient in (2.10) to produce a new effective (non-dimensional) bulk potential in (2.18), namely

$$\widetilde{\psi}(Q) = a_0 - \frac{a_2 - 4\ell_1\eta^2\tau_0^2}{2}\mathrm{tr}(Q^2) - \frac{a_3}{3}\mathrm{tr}(Q^3) + \frac{a_4}{4}\big(\mathrm{tr}(Q^2)\big)^2, \tag{2.23}$$

where $\widetilde{a_2} = a_2 - 4\eta^2\tau_0^2$ is the coefficient in front of $\mathrm{tr}(Q^2)$. If $\tau_0 = 15$ and $a_2 = 1$, for instance, then choosing $\eta = 0.0408$ yields $\widetilde{a_2} \approx 0.5$, which is a significant change in the global minimum. One would have to choose $\eta = 0.01$ to have $\widetilde{a_2} > 0.9$. Moreover, if η is not small enough to compensate for τ_0, then $\widetilde{a_2}$ will be negative, which makes the $\mathrm{tr}(Q^2)$ term positive. If $\widetilde{a_2}$ is sufficiently large and negative, then $\widetilde{\psi}(Q)$ will be a convex function, with a single minimum at $Q = 0$, implying that the isotropic phase is preferred. Furthermore, in the case of thermotropic LCs, the $\mathrm{tr}(Q^2)$ coefficient depends on temperature.

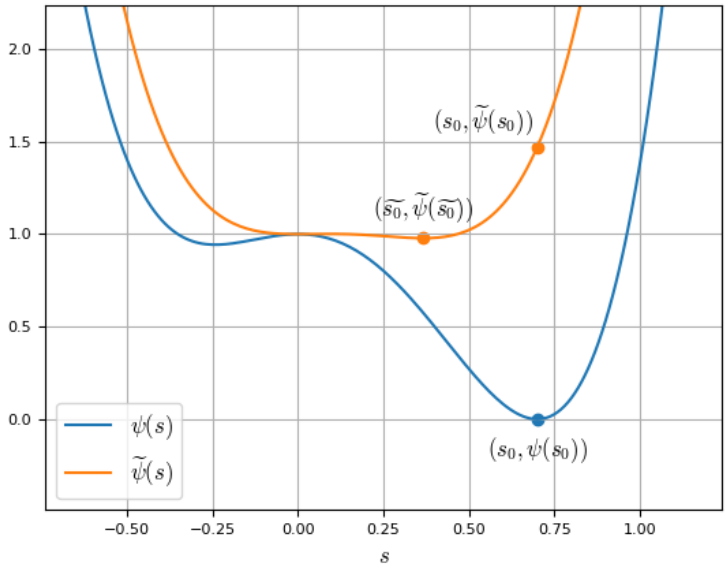

Figure 2.2. The two double wells from the two models. This compares the double well ψ in (2.10) to the effective double well $\widetilde{\psi}$ in (2.23), which arises when the alternate cholesteric model is used. Notice that the global minima, s_0 for ψ and $\widetilde{s_0}$ for $\widetilde{\psi}$, of the two bulk potentials differ greatly.

Thus, using (2.19) for the elastic energy leads to the effect that increasing the twist parameter is akin to increasing the temperature, which is not consistent with experiments. Figure 2.2 shows a comparison between the original double well and the modified one; clearly, the location of the global minima are different.

Hence, a moderate twist will change the effective double well (bulk) potential, which directly controls the nematic phase diagram of the LC; the severity of the change increases with the twist. To the best of our knowledge, the material doping discussed at the beginning of Section 2.4, which is needed to create a cholesteric LC, should not change the nematic phase diagram, which is directly connected to the double well potential. Moreover, choosing η sufficiently small to reduce the interference with the bulk potential is computationally inconvenient because it makes the problem more stiff; smaller time-steps

will be needed to ensure energy decrease in a gradient descent scheme. Therefore, we mainly adopt the approach in [78], which is justified in [68], and simply drop the $\mathrm{tr}(Q^2)$ term in (2.21). But we do provide a comparison with the model in [88] in Section 5.6.

Remark 3. *The surface anchoring energy proposed in [88] is the same as that given in* (2.12), (2.13) *but with a trivial change in the constants.*

Chapter 3. Minimizing the Landau-de Gennes Energy

Existence of a minimizer of (2.18) can be established through the direct method of the calculus of variations; for instance, see [30]. Computing a minimizer can, in principle, be done by solving the Euler-Lagrange equations associated with (2.18) (i.e. the first order condition). However, these equations are non-linear and the energy is non-convex, so simply applying Newton's method will not necessarily converge nor produce a minimizer.

We begin by developing a weak formulation of the first order condition. Then, we describe multiple gradient flow schemes for finding (local) minimizers. The main purpose is to explain how different choices of the scheme (i.e. different implicit-explicit splittings) require different time step restrictions that are affected by the bulk and boundary parameters η and ω, and the twist parameter τ_0.

3.1. Existence of a Minimizer

The minimization problem for the LdG energy functional (2.18), and associated first order condition, is

$$\bar{Q} = \underset{Q \in \mathbf{V}}{\arg\min}\, \mathcal{E}[Q], \qquad \delta_Q \mathcal{E}[\bar{Q}; P] = 0, \qquad \forall P \in \mathbf{V}, \tag{3.1}$$

where $\mathbf{V} := H^1(\Omega; \mathbf{S}_0)$ is the admissible space and $\delta_Q \mathcal{E}[\cdot;\cdot]$ is the variational derivative of $\mathcal{E}[\cdot]$. Note that $\mathbf{S}_0$ can be uniquely identified with a five dimensional vector space [42], i.e. there exists 3×3, symmetric traceless basis matrices $\{E^i\}_{i=1}^5$ such that any $Q \in \mathbf{S}_0$ can be uniquely expressed as $Q = q_i E^i$, for some coefficients $q_1, \ldots, q_5$. Therefore, $\mathbf{V}$ is isomorphic to $H^1(\Omega; \mathbb{R}^5)$.

Existence of a minimizer requires the energy to be bounded from below. To show this, we introduce various bilinear forms that will be convenient in our analysis. The fol-

lowing theorem [30, Lem. 4.1] establishes this result for the ℓ_1, ℓ_2, ℓ_3 terms in the elastic energy.

Theorem 4. *Let $a_e(\cdot,\cdot) : \mathbf{V} \times \mathbf{V} \to \mathbb{R}$ be the symmetric bilinear form defined by*

$$a_e(Q,P) := \ell_1 (Q_{ij,k}, P_{ij,k})_\Omega + \ell_2 (Q_{ij,j}, P_{ik,k})_\Omega + \ell_3 (Q_{ij,k}, P_{ik,j})_\Omega . \tag{3.2}$$

Then $a_e(\cdot,\cdot)$ is bounded. If ℓ_1, ℓ_2, ℓ_3 satisfy

$$0 < \ell_1, \quad -\ell_1 < \ell_3 < 2\ell_1, \quad -\frac{3}{5}\ell_1 - \frac{1}{10}\ell_3 < \ell_2, \tag{3.3}$$

then there is a constant $c > 0$ such that $a_e(P,P) \geq c\|\nabla P\|^2_{0,\Omega}$ for all $P \in \mathbf{V}$.

Proposition 5 (Coercivity)**.** *Let $a_s(\cdot,\cdot) : \mathbf{V} \times \mathbf{V} \to \mathbb{R}$ be the symmetric bilinear form defined by*

$$a_s(Q,P) = w_0 (Q,P)_\Gamma + w_1 \left(Q - Q^\perp, P\right)_\Gamma . \tag{3.4}$$

There exists a constant $\alpha_1 > 0$ such that

$$a_e(P,P) + a_s(P,P) \geq \alpha_1 \|P\|^2_{1,\Omega}, \qquad \forall P \in \mathbf{V}. \tag{3.5}$$

Proof. We start by noting that it is clear from (3.4) that

$$a_{\mathrm{s}}(P,P) \geq w_0 \|P\|^2_{0,\Gamma}.$$

Now, we compute the following inequality. Let $\mathbf{r}(\mathbf{x}) := \mathbf{x} - \mathbf{x}_0$, where $\mathbf{x}_0$ is the central point in Ω, i.e. the point such that

$$\max_{\mathbf{x}\in\Omega} |\mathbf{r}(\mathbf{x})| = (1/2)\operatorname{diam}\Omega =: r^*.$$

Now, for each $i \in \{1,2,3\}$ the spatial derivative with respect to i of the ith component of

$\mathbf{r}$ is 1, so $|\nabla \cdot \mathbf{r}| = 3$. And so, for any symmetric traceless tensor P we have

$$\begin{aligned}
\|P\|_{0,\Omega}^2 &= \frac{1}{3}\left(|\nabla \cdot \mathbf{r}||P|^2, 1\right)_\Omega \\
&= -\frac{1}{3}\left(\mathbf{r} \cdot \nabla(|P|^2), 1\right)_\Omega + \frac{1}{3}\left((\boldsymbol{\nu} \cdot \mathbf{r})|P|^2, 1\right)_\Gamma \\
&= -\frac{2}{3}\left(P_{ij}P_{ij,k}r_k, 1\right)_\Omega + \frac{1}{3}\left(\nu_k r_k P_{ij}P_{ij}, 1\right)_\Gamma \\
&\leq \frac{2}{3}\left(|\mathbf{r}||P||\nabla P|, 1\right)_\Omega + \frac{1}{3}\left(|\mathbf{r}||P|^2, 1\right)_\Gamma \\
&\leq \frac{2r^*}{3}\left(|P||\nabla P|, 1\right)_\Omega + \frac{r^*}{3}\left(|P|^2, 1\right)_\Gamma \\
&\leq \frac{r^*\delta}{3}\|P\|_{0,\Omega}^2 + \frac{r^*\delta^{-1}}{3}\|\nabla P\|_{0,\Omega}^2 + \frac{r^*}{3}\|P\|_{0,\Gamma}^2 \\
&= (1/2)\|P\|_{0,\Omega}^2 + (2/9)(r^*)^2\|\nabla P\|_{0,\Omega}^2 + (1/3)r^*\|P\|_{0,\Gamma}^2,
\end{aligned}$$

where we have chosen $\delta = 3/2r^*$. This establishes that

$$\|P\|_{0,\Omega}^2 \leq (4/9)(r^*)^2\|\nabla P\|_{0,\Omega}^2 + (2/3)r^*\|P\|_{0,\Gamma}^2 \leq (4/9)r^*\max\{r^*, 3/2\}\left[\|\nabla P\|_{0,\Omega}^2 + \|P\|_{0,\Gamma}^2\right],$$

Therefore,

$$\begin{aligned}
a_{\mathrm{e}}(P,P) + a_{\mathrm{s}}(P,P) &\geq \alpha_0\|\nabla P\|_{0,\Omega}^2 + w_0\|P\|_{0,\Gamma}^2 \\
&\geq \frac{\alpha_0}{2}\|\nabla P\|_{0,\Omega}^2 + \min\{\alpha_0/2, w_0\}\left[\|\nabla P\|_{0,\Omega}^2 + \|P\|_{0,\Gamma}^2\right] \\
&\geq \frac{\alpha_0}{2}\|\nabla P\|_{0,\Omega}^2 + \frac{\min\{\alpha_0/2, w_0\}}{(4/9)r^*\max\{r^*, 3/2\}}\|P\|_{0,\Omega}^2 \\
&\geq \min\left\{\frac{\alpha_0}{2}, \frac{9\min\{\alpha_0/2, w_0\}}{4r^*\max\{r^*, 3/2\}}\right\}\|P\|_{1,\Omega}^2 \\
&=: \alpha_1\|P\|_{1,\Omega}^2.
\end{aligned}$$

□

We also have the bilinear form $a_{\mathrm{t}}(\cdot,\cdot) : \mathbf{V} \times \mathbf{V} \to \mathbb{R}$, which is *not* coercive, accounting for the twist term:

$$a_{\mathrm{t}}(Q,P) := 2\ell_1\tau_0\left[\varepsilon_{ikl}\left(Q_{jk,l}, P_{ij}\right)_\Omega + \varepsilon_{ikl}\left(P_{jk,l}, Q_{ij}\right)_\Omega\right], \tag{3.6}$$

and can be bounded by first noting:

$$\begin{aligned}\left|\varepsilon_{ikl}\left(Q_{jk,l},P_{ij}\right)_{\Omega}\right| &\leq \sum_{ijkl}\left(|\varepsilon_{ikl}||Q_{jk,l}|,|P_{ij}|\right)_{\Omega}\\ &\leq \sum_{ijkl}\left(|Q_{jk,l}|,|P_{ij}|\right)_{\Omega} \leq \sum_{ijkl}\|Q_{jk,l}\|_{0,\Omega}\|P_{ij}\|_{0,\Omega}\\ &\leq \sum_{ikl}\left(\sum_{m}\|Q_{mk,l}\|_{0,\Omega}^{2}\right)^{1/2}\left(\sum_{n}\|P_{in}\|_{0,\Omega}^{2}\right)^{1/2}\\ &\leq \left(3^{3}\right)^{1/2}\left(\sum_{mkl}\|Q_{mk,l}\|_{0,\Omega}^{2}\right)^{1/2}\left(\sum_{in}\|P_{in}\|_{0,\Omega}^{2}\right)^{1/2}\\ &= \sqrt{27}\cdot|Q|_{1,\Omega}\|P\|_{0,\Omega},\end{aligned} \tag{3.7}$$

which implies that

$$\begin{aligned}a_{\mathrm{t}}\left(Q,P\right) &= 2\ell_{1}\tau_{0}\varepsilon_{ikl}\left[\left(Q_{jk,l},P_{ij}\right)_{\Omega}+\left(P_{jk,l},Q_{ij}\right)_{\Omega}\right]\\ &\leq 2\ell_{1}\tau_{0}\sqrt{27}\left[|Q|_{1,\Omega}\|P\|_{0,\Omega}+|P|_{1,\Omega}\|Q\|_{0,\Omega}\right].\end{aligned} \tag{3.8}$$

For later use, we define one bilinear form to contain (3.2), (3.4), and (3.6):

$$a\left(Q,P\right)=a_{\mathrm{e}}\left(Q,P\right)+a_{\mathrm{t}}\left(Q,P\right)+a_{\mathrm{s}}\left(Q,P\right), \tag{3.9}$$

which satisfies the following continuity result.

Proposition 6 (Continuity)**.** *There holds*

$$\begin{aligned}&a_{e}\left(Q,P\right)\leq c_{e}|Q|_{1,\Omega}|P|_{1,\Omega},\quad a_{t}\left(Q,P\right)\leq c_{t}\|Q\|_{1,\Omega}\|P\|_{1,\Omega},\\ &a_{s}\left(Q,P\right)\leq c_{s}\|Q\|_{0,\Gamma}\|P\|_{0,\Gamma},\quad a\left(Q,P\right)\leq c_{0}\|Q\|_{1,\Omega}\|P\|_{1,\Omega},\end{aligned} \tag{3.10}$$

for all $Q,P\in\mathbf{V}$*, where*

$$c_{e}=\ell_{1}+3\ell_{2}+\ell_{3},\ c_{t}=2\sqrt{27}\ell_{1}\tau_{0},\ c_{s}=w_{0}+3w_{1},\ c_{0}=c_{e}+c_{t}+\beta_{3}c_{s}, \tag{3.11}$$

where $\beta_{3}>0$ *is a trace embedding constant depending on* Ω*.*

Proof. Let Q, P be arbitrary in $\mathbf{V}$. By the Cauchy-Schwarz inequality, we have

$$\begin{aligned} a_{\mathrm{e}}(Q,P) &= \ell_1 (Q_{ij,k}, P_{ij,k})_\Omega + \ell_2 (Q_{ij,j}, P_{ik,k})_\Omega + \ell_3 (Q_{ij,k}, P_{ik,j})_\Omega \\ &\leq \ell_1 |Q|_{1,\Omega}|P|_{1,\Omega} + 3\ell_2 |Q|_{1,\Omega}|P|_{1,\Omega} + \ell_3 |Q|_{1,\Omega}|P|_{1,\Omega} \\ &\leq (\ell_1 + 3\ell_2 + \ell_3)|Q|_{1,\Omega}|P|_{1,\Omega}. \end{aligned}$$

Applying a simple Cauchy-Schwarz estimate to (3.8), we get

$$a_{\mathrm{t}}(Q,P) \leq 2\sqrt{27}\ell_1\tau_0 \|Q\|_{1,\Omega}\|P\|_{1,\Omega}.$$

The surface anchoring term satisfies

$$\begin{aligned} a_{\mathrm{s}}(Q,P) &= w_0 (Q,P)_\Gamma + w_1 \left(Q - Q^\perp, P\right)_\Gamma \\ &\leq (w_0 + 3w_1)\|Q\|_{0,\Gamma}\|P\|_{0,\Gamma}, \end{aligned}$$

which can be shown by keeping in mind that

$$|Q^\perp : P| \leq |Q^\perp||P| \leq |\Pi|^2|Q||P| = 2|Q||P|,$$

where $\Pi := \boldsymbol{\nu} \otimes \boldsymbol{\nu} - I$ is the projection tensor. Combining these inequalities, and using a trace theorem, the proof is complete. □

Next, consider the following sub-part of the energy (2.18):

$$\begin{aligned} \widetilde{\mathcal{E}}[Q] &:= \int_\Omega f(Q, \nabla Q)\, d\mathbf{x} + \frac{1}{\eta^2}\int_\Omega \psi(Q)\, d\mathbf{x}, \\ &\equiv \frac{1}{2}a_{\mathrm{e}}(Q,Q) + \frac{1}{2}a_{\mathrm{t}}(Q,Q) + \frac{1}{\eta^2}\int_\Omega \psi(Q)\, d\mathbf{x}. \end{aligned} \tag{3.12}$$

Combining Theorem 4 with the form of the energy in (2.18) and other basic results (see [30, Lem. 4.2, Thm. 4.3] for instance) we arrive at the following result.

Theorem 7 (existence of a minimizer)**.** *Let $\widetilde{\mathcal{E}}$ be given by* (3.12)*, where ψ is given by* (2.10)*. Furthermore, let τ_0 be bounded and assume that ℓ_1, ℓ_2, ℓ_3 satisfy* (3.3)*. Then $\widetilde{\mathcal{E}}$ has a minimizer in the space $\mathbf{V}$. Furthermore, $\mathcal{E}$ in* (2.18)*, with g and ϕ given by* (2.12)*, and χ a bounded linear functional on $\mathbf{V}$, has a minimizer in $\mathbf{V}$.*

Proof. When $\tau_0 = 0$, the result essentially follows from [30, Lem. 4.2, Thm. 4.3]. Otherwise, consider the case where $\tau_0 \neq 0$. Using Theorem 4, we have that $\widetilde{\mathcal{E}}$ satisfies the bound

$$\begin{aligned}\widetilde{\mathcal{E}}[Q] &= \frac{1}{2}\int_\Omega \ell_1|\nabla Q|^2 + \ell_2(\nabla\cdot Q)^2 + \ell_3(\nabla Q)^\dagger \vdots \nabla Q \, d\mathbf{x} \\ &\quad + 2\tau_0 \int_\Omega \nabla Q \vdots (\varepsilon \cdot Q)\, d\mathbf{x} + \frac{1}{\eta^2}\int_\Omega \psi(Q)\, d\mathbf{x} \\ &\geq \frac{c}{2}\int_\Omega |\nabla Q|^2\, d\mathbf{x} + 2\tau_0 \int_\Omega \nabla Q \vdots (\varepsilon \cdot Q)\, d\mathbf{x} + \frac{1}{\eta^2}\int_\Omega \psi(Q)\, d\mathbf{x},\end{aligned} \tag{3.13}$$

for all $Q \in \mathbf{V}$, for some constant $c > 0$. Furthermore, one can show

$$\widetilde{\mathcal{E}}[Q] \geq \frac{1}{2}(c - \zeta_0)\int_\Omega |\nabla Q|^2\, d\mathbf{x} - \frac{c'}{\zeta_0}\int_\Omega |Q|^2\, d\mathbf{x} + \frac{1}{\eta^2}\int_\Omega \psi(Q)\, d\mathbf{x}, \tag{3.14}$$

for any $\zeta_0 > 0$ where $c' > 0$ is some bounded constant. Choosing $\zeta_0 = c/2$, we get

$$\widetilde{\mathcal{E}}[Q] \geq \frac{c}{4}\int_\Omega |\nabla Q|^2\, d\mathbf{x} + \frac{1}{\eta^2}\int_\Omega \widehat{\psi}(Q)\, d\mathbf{x}, \tag{3.15}$$

where $\widehat{\psi}(Q) := \psi(Q) - 2\eta^2(c'/c)|Q|^2$. Thus, $\widetilde{\mathcal{E}}[Q]$ is clearly bounded below by a coercive energy on $\mathbf{V}$. By standard calculus of variations [20, 55], there exists a minimizer, $\widehat{Q}$, of $\widetilde{\mathcal{E}}[\cdot]$ in $\mathbf{V}$. The same holds true for $\mathcal{E}[\cdot]$. □

For convenience, we collect all linear terms in $\delta_Q\mathcal{E}[Q;P]$ into a single linear form, denoted l_{rhs}:

$$l_{\text{rhs}}(P) = (\chi(P),1)_\Omega + w_0\,(Q_\Gamma, P)_\Gamma + w_1\left(-\frac{s_0}{3}\boldsymbol{\nu}\otimes\boldsymbol{\nu}, P\right)_\Gamma. \tag{3.16}$$

Using (3.9) and (3.16), we can now write $\mathcal{E}[Q]$ in the form

$$\mathcal{E}[Q] = (1/2)a\,(Q,Q) + (1/\eta^2)\,(\psi(Q),1)_\Omega + (1/\omega)\,(\phi(Q),1)_\Gamma - l_{\rm rhs}(Q), \tag{3.17}$$

which yields the following expression for the first variation of $\mathcal{E}$:

$$\delta_Q\mathcal{E}[Q;P] = a\,(Q,P) + (1/\eta^2)\,(D\psi(Q),P)_\Omega + (1/\omega)\,(D\phi(Q),P)_\Gamma - l_{\rm rhs}(P). \tag{3.18}$$

The full strong form for the non-dimensional LdG model consists of a tensor-valued, elliptic partial differential equation (PDE) defined over Ω with a tensor-valued Robin boundary condition. In terms of indices, $1 \le i,j \le 3$, the bulk PDE is (with χ taken as in (2.15), e.g.)

$$\begin{aligned} &-\ell_1 Q_{ij,kk} - \ell_2 Q_{ik,kj} - \ell_3 Q_{ik,jk} - 4\ell_1\tau_0\varepsilon_{i\ell k}Q_{\ell j,k} \\ &\qquad + \frac{1}{\eta^2}\bigg(- a_2 Q_{ij} - a_3 (Q^2)_{ij} + a_4 |Q|^2 Q_{ij}\bigg) = -\frac{1}{2}\varepsilon_{\rm a}(\mathbf{E}\otimes\mathbf{E})_{ij}, \quad \text{in } \Omega, \end{aligned} \tag{3.19}$$

where only the traceless part of the tensor equation is considered. The boundary condition is given by

$$\begin{aligned} &\ell_1\nu_k Q_{ij,k} + \ell_2\nu_j Q_{ik,k} + \ell_3\nu_k Q_{ik,j} + 2\ell_1\tau_0\nu_k\varepsilon_{i\ell k}Q_{\ell j} + w_0 Q_{ij} + w_1(Q_{ij} - Q^\perp_{ij}) \\ &\qquad + \frac{1}{\omega}\bigg(|Q|^2 - \frac{2(s_0)^2}{3}\bigg)Q_{ij} = w_0(Q_\Gamma)_{ij} - \frac{w_1 s_0}{3}\nu_i\nu_j, \quad \text{on } \Gamma, \end{aligned} \tag{3.20}$$

where, again, only the traceless part is considered. In (3.19), note that the term $4\ell_1\tau_0\varepsilon_{i\ell k}Q_{\ell j,k}$ is analogous to a convective term, e.g. $(V\cdot\nabla)Q$, where $V_{i\ell k} = 4\ell_1\tau_0\varepsilon_{i\ell k}$ is like a "velocity". It is well known [85] that convection-diffusion problems present some difficulties in their numerical approximation, especially when the velocity is large. This is the case here when τ_0 is large, which manifests as a mesh-size restriction in Thm. 13, as well as restricting the time-step when a popular convex-splitting scheme is used for finding an energy minimum (see Thm. 11).

3.2. Continuous Gradient Flow

We look for an energy minimizer using a gradient flow strategy [61, 78, 100, 8, 19] applied to the energy (2.18). Let t represent "time" and suppose that $Q \equiv Q(x,t)$ evolves by an $L^2(\Omega)$ gradient flow:

$$(\partial_t Q(\cdot,t), P)_\Omega = -\delta_Q \mathcal{E}[Q;P], \quad \forall P \in \mathbf{V}, \tag{3.21}$$

where $Q(x,0) = Q_0 \in \mathbf{V}$ is the initial guess for the flow. Formally, the solution of (3.21) will converge to $Q_* := \lim_{t\to\infty} Q(\cdot,t)$, which is a local minimizer of $\mathcal{E}$. In this case, $Q(x,t)$ satisfies a parabolic PDE (in strong form), and by the standard theory of parabolic PDEs [41, 57], it has a unique solution. Gradient flows are related to the natural relaxation that many physical systems undergo, including LCs, which is why we use it in our simulations. Directly minimizing $\mathcal{E}$ by some other optimization technique is also possible and may yield other minimizers that are not commonly observed in experiment.

If ψ is the Landau-de Gennes bulk potential in (2.10), and we use the one-constant elastic energy, then (3.21) is essentially a tensor-valued Allen-Cahn type of equation, i.e.

$$(\partial_t Q(\cdot,t))_{ij} - \Delta Q_{ij} + (D\psi(Q))_{ij} = 0, \text{ in } \Omega, \text{ for } t > 0, \quad \forall i,j = 1,2,3. \tag{3.22}$$

By the standard theory of parabolic PDEs [41, 57], it has a unique solution.

3.3. Discrete Gradient Flow

We discretize (3.21) in time by first letting $Q_k(x) \approx Q(x, k\delta t)$, where $\delta t > 0$ is a finite time-step and k is the time index. Next, we replace $\partial_t Q(\cdot,t)$ by a finite difference approximation, so then (3.21) becomes a sequence of elliptic problems. In other words,

given Q_k, find $Q_{k+1} \in \mathbf{V}$ such that

$$\delta t^{-1} \left(Q_{k+1} - Q_k, P\right)_{\delta t} = -\delta_Q \mathcal{E}[Q_{k+1}; P], \quad \forall P \in \mathbf{V}, \tag{3.23}$$

where we have defined a time-stepping inner product $(\cdot, \cdot)_{\delta t}$ by

$$(P, T)_{\delta t} := \frac{1}{\eta^2} (P, T)_\Omega + \frac{1}{\omega} (P, T)_\Gamma . \tag{3.24}$$

We also define a norm by $\|P\|_{\delta t}^2 := (P, P)_{\delta t}$. One can show that (3.26) is equivalent to a minimizing movements strategy [67]:

$$Q_{k+1} = \underset{Q \in \mathbf{V}}{\arg\min}\, \mathcal{F}^k(Q), \quad \mathcal{F}^k(Q) := \frac{1}{2\delta t} \|Q - Q_k\|_{\delta t}^2 + \mathcal{E}[Q], \tag{3.25}$$

which immediately yields the useful property $\mathcal{F}^k(Q_{k+1}) \leq \mathcal{F}^k(Q_k) \leq \mathcal{F}^{k-1}(Q_k)$ and implies that $\mathcal{E}[Q_{k+1}] \leq \mathcal{E}[Q_k]$ for all k. However, (3.23) is a *fully implicit* equation and requires an iterative solution because of the non-linearities in $\psi(Q)$ and $\phi(Q)$.

3.3.1. Fully implicit gradient descent

The fully implicit gradient descent scheme given by (3.23) may be explicitly written as follows. Given $Q_k \in \mathbf{V}$, we seek $Q_{k+1} \in \mathbf{V}$ such that

$$\begin{aligned} \delta t^{-1} \left(Q_{k+1} - Q_k, P\right)_{\delta t} + a\left(Q_{k+1}, P\right) + (1/\eta^2) \left(D\psi(Q_{k+1}), P\right)_\Omega \\ + (1/\omega) \left(D\phi(Q_{k+1}), P\right)_\Gamma = l_{\text{rhs}}(P), \quad \forall P \in \mathbf{V}. \end{aligned} \tag{3.26}$$

Starting from an initial guess Q_0, we iterate (3.26) until we reach a final iteration index or some other stopping criteria (see Section 5.1). Note that Newton's method is required for solving (3.26) because of ψ and ϕ. The following theorem gives a time-step restriction to ensure energy decrease.

Theorem 8. *The sequence* $\{Q_k\}_{k=0}^{\infty}$ *defined by the method in* (3.26) *is monotonically energy decreasing, i.e.*

$$\mathcal{E}[Q_{k+1}] \leq \mathcal{E}[Q_k],$$

provided that

$$\delta t \leq 2/\max\{a_2 + a_3^2/a_4, 2s_0^2/3\}. \tag{3.27}$$

Proof. We start with the following inequality for any $P, T \in \mathbf{V}$ (recall that $a_2, a_3, a_4 > 0$):

$$\begin{aligned}
\left(T, D^2\psi(P)T\right)_\Omega &= -a_2\|T\|_{0,\Omega}^2 - 2a_3\left(PT, T\right)_\Omega + 2a_4\left(P:T, P:T\right)_\Omega + a_4\left(|T|^2, |P|^2\right)_\Omega \\
&\geq -a_2\|T\|_{0,\Omega}^2 - (a_3\delta)\left(|T|^2, |P|^2\right)_\Omega - (a_3/\delta)\|T\|_{0,\Omega}^2 + a_4\left(|T|^2, |P|^2\right)_\Omega \\
&= -(a_2 + a_3^2/a_4)\|T\|_{0,\Omega}^2 = -a'\|T\|_{0,\Omega}^2,
\end{aligned} \tag{3.28}$$

by choosing $\delta = a_4/a_3$, where $a' = a_2 + a_3^2/a_4$. Similarly, we have

$$\begin{aligned}
\left(T, D^2\phi(P)T\right)_\Gamma &= (-2s_0^2/3)\|T\|_{0,\Gamma}^2 + 2\left(P:T, P:T\right)_\Gamma + \left(|T|^2, |P|^2\right)_\Gamma \\
&\geq (-2s_0^2/3)\|T\|_{0,\Gamma}^2 = -s'\|T\|_{0,\Gamma}^2,
\end{aligned} \tag{3.29}$$

where $s' = 2s_0^2/3$. Next, setting $S_{k+1} := Q_{k+1} - Q_k$, we have the identity:

$$a\left(Q_k, Q_k\right) = a\left(Q_{k+1}, Q_{k+1}\right) + a\left(S_{k+1}, S_{k+1}\right) - 2a\left(S_{k+1}, Q_{k+1}\right). \tag{3.30}$$

Note also that, substituting $P = S_{k+1}$ into (3.26), we have

$$\begin{aligned}
\delta t^{-1}\left(S_{k+1}, S_{k+1}\right)_{\delta t} &= -a\left(Q_{k+1}, S_{k+1}\right) - (1/\eta^2)\left(D\psi(Q_{k+1}), S_{k+1}\right)_\Omega \\
&\quad - (1/\omega)\left(D\phi(Q_{k+1}), S_{k+1}\right)_\Gamma + l_{\text{rhs}}(S_{k+1}).
\end{aligned} \tag{3.31}$$

Now use a Taylor expansion of $\psi(Q_k)$ and $\phi(Q_k)$ about Q_{k+1}, i.e. set $\bar{Q}(s) := (1-s)Q_{k+1} +$

sQ_k, and for some $s_1, s_2 \in (0,1)$ we obtain from (3.17) combined with (3.28), (3.29), (3.30):

$$\begin{aligned}
\mathcal{E}[Q_k] &= (1/2)a\left(Q_k, Q_k\right) + (1/\eta^2)\left(\psi(Q_{k+1}), 1\right)_\Omega + (1/\omega)\left(\phi(Q_{k+1}), 1\right)_\Gamma \\
&\quad - l_{\mathrm{rhs}}(Q_{k+1}) + l_{\mathrm{rhs}}(S_{k+1}) - (1/\eta^2)\left(D\psi(Q_{k+1}), S_{k+1}\right)_\Omega \\
&\quad - (1/\omega)\left(D\phi(Q_{k+1}), S_{k+1}\right)_\Gamma + (1/(2\eta^2))\left(S_{k+1}, D^2\psi(\bar{Q}(s_1))S_{k+1}\right)_\Omega \\
&\quad + (1/(2\omega))\left(S_{k+1}, D^2\phi(\bar{Q}(s_2))S_{k+1}\right)_\Gamma \\
&\geq (1/2)a\left(Q_{k+1}, Q_{k+1}\right) + (1/\eta^2)\left(\psi(Q_{k+1}), 1\right)_\Omega + (1/\omega)\left(\phi(Q_{k+1}), 1\right)_\Gamma \\
&\quad - l_{\mathrm{rhs}}(Q_{k+1}) + (1/2)a\left(S_{k+1}, S_{k+1}\right) - a\left(S_{k+1}, Q_{k+1}\right) + l_{\mathrm{rhs}}(S_{k+1}) \\
&\quad - (1/\eta^2)\left(D\psi(Q_{k+1}), S_{k+1}\right)_\Omega - (1/\omega)\left(D\phi(Q_{k+1}), S_{k+1}\right)_\Gamma \\
&\quad - (1/\eta^2)(a'/2)\|S_{k+1}\|^2_{0,\Omega} - (1/\omega)(s'/2)\|S_{k+1}\|^2_{0,\Gamma}.
\end{aligned}$$

We then substitute (3.31) into the above line and use (3.17) again to see that

$$\begin{aligned}
\mathcal{E}[Q_k] &\geq \mathcal{E}[Q_{k+1}] + \delta t^{-1}\left(S_{k+1}, S_{k+1}\right)_{\delta t} - (1/\eta^2)(a'/2)\|S_{k+1}\|^2_{0,\Omega} - (1/\omega)(s'/2)\|S_{k+1}\|^2_{0,\Gamma} \\
&= \mathcal{E}[Q_{k+1}] + (1/\eta^2)\left(\frac{1}{\delta t} - \frac{a'}{2}\right)\|S_{k+1}\|^2_{0,\Omega} + (1/\omega)\left(\frac{1}{\delta t} - \frac{s'}{2}\right)\|S_{k+1}\|^2_{0,\Gamma} \geq \mathcal{E}[Q_{k+1}],
\end{aligned}$$

provided that $\delta t \leq 2/\max\{a', s'\}$. □

The time step restriction in (3.27) involves non-dimensional constants of $O(1)$. However, the time step inner product (3.24) used in (3.26) accounts for the strength of the non-convex terms through the positive constants η and ω. In other words, when either η and ω are small, the minimizing movements scheme in (3.25) penalizes $Q_{k+1} - Q_k$ to be small. Hence, the minimization sequence will take more iterations when either η and ω are small.

3.3.2. Implicit-explicit gradient descent

Other types of time-discretizations can be used, but they usually have more stringent time-step restrictions. The first of these that we shall discuss is the *implicit-explicit* gradient descent method, which is as follows. Given $Q_k \in \mathbf{V}$, we seek $Q_{k+1} \in \mathbf{V}$ that solves the following linear equation:

$$\begin{aligned} \delta t^{-1} \left(Q_{k+1} - Q_k, P\right)_{\delta t} + a\left(Q_{k+1}, P\right) + \left(1/\eta^2\right) \left(D\psi(Q_k), P\right)_{\Omega} \\ + \left(1/\omega\right) \left(D\phi(Q_k), P\right)_{\Gamma} = l_{\mathrm{rhs}}(P), \qquad \forall P \in \mathbf{V}. \end{aligned} \tag{3.32}$$

Theorem 9. *Assume the sequence $\{Q_k\}_{k=0}^{\infty}$ defined by the method in* (3.32) *enjoys the additional regularity $|Q_k| \in L^{\infty}(\Omega)$ for all $k \geq 0$. Then, the sequence is monotonically energy decreasing, i.e.*

$$\mathcal{E}[Q_{k+1}] \leq \mathcal{E}[Q_k],$$

if δt is small enough.

Proof. We first note that, similarly to the fully implicit case, we substitute $P = S_{k+1} := Q_{k+1} - Q_k$ into (3.32) and have

$$\begin{aligned} \delta t^{-1} \left(S_{k+1}, S_{k+1}\right)_{\delta t} = -a\left(Q_{k+1}, S_{k+1}\right) - \left(1/\eta^2\right) \left(D\psi(Q_k), S_{k+1}\right)_{\Omega} \\ - \left(1/\omega\right) \left(D\phi(Q_k), S_{k+1}\right)_{\Gamma} + l_{\mathrm{rhs}}(S_{k+1}). \end{aligned} \tag{3.33}$$

Using a Taylor expansion of $\psi(Q_{k+1})$ and $\phi(Q_{k+1})$ about Q_k (analogous to the fully implicit case, i.e. using $\bar{Q}(s)$ defined in the proof of Theorem 8), we find that for some

$s_1, s_2 \in (0,1)$ we obtain from (3.17) combined with a slightly rearranged (3.30):

$$\begin{aligned}
\mathcal{E}[Q_{k+1}] &= (1/2)a\left(Q_{k+1}, Q_{k+1}\right) + (1/\eta^2)\left(\psi(Q_k), 1\right)_\Omega + (1/\omega)\left(\phi(Q_k), 1\right)_\Gamma \\
&\quad - l_{\text{rhs}}(Q_k) - l_{\text{rhs}}(S_{k+1}) + (1/\eta^2)\left(D\psi(Q_k), S_{k+1}\right)_\Omega \\
&\quad + (1/\omega)\left(D\phi(Q_k), S_{k+1}\right)_\Gamma + (1/(2\eta^2))\left(S_{k+1}, D^2\psi(\bar{Q}(s_1))S_{k+1}\right)_\Omega \\
&\quad + (1/(2\omega))\left(S_{k+1}, D^2\phi(\bar{Q}(s_2))S_{k+1}\right)_\Gamma \\
&\leq (1/2)a\left(Q_k, Q_k\right) + (1/\eta^2)\left(\psi(Q_k), 1\right)_\Omega + (1/\omega)\left(\phi(Q_k), 1\right)_\Gamma \\
&\quad - l_{\text{rhs}}(Q_k) - (1/2)a\left(S_{k+1}, S_{k+1}\right) + a\left(S_{k+1}, Q_{k+1}\right) - l_{\text{rhs}}(S_{k+1}) \\
&\quad + (1/\eta^2)\left(D\psi(Q_k), S_{k+1}\right)_\Omega + (1/\omega)\left(D\phi(Q_k), S_{k+1}\right)_\Gamma \\
&\quad + (1/\eta^2)(\overline{D^2\psi}/2)\|S_{k+1}\|^2_{0,\Omega} + (1/\omega)(\overline{D^2\phi}/2)\|S_{k+1}\|^2_{0,\Gamma},
\end{aligned}$$

where $\overline{D^2\psi} := \|D^2\psi(\bar{Q}(s_1))\|_{0,\infty,\Omega}$ and $\overline{D^2\phi} := \|D^2\phi(\bar{Q}(s_2))\|_{0,\infty,\Gamma}$. We then substitute (3.33) into the above and again use (3.17) to see that

$$\begin{aligned}
\mathcal{E}[Q_{k+1}] &\leq \mathcal{E}[Q_k] - \delta t^{-1}\left(S_{k+1}, S_{k+1}\right)_{\delta t} + (1/\eta^2)(\overline{D^2\psi}/2)\|S_{k+1}\|^2_{0,\Omega} \\
&\quad + (1/\omega)(\overline{D^2\phi}/2)\|S_{k+1}\|^2_{0,\Gamma} \\
&= \mathcal{E}[Q_k] + (1/\eta^2)\left(\frac{\overline{D^2\psi}}{2} - \frac{1}{\delta t}\right)\|S_{k+1}\|^2_{0,\Omega} \\
&\quad + (1/\omega)\left(\frac{\overline{D^2\phi}}{2} - \frac{1}{\delta t}\right)\|S_{k+1}\|^2_{0,\Gamma} \\
&\leq \mathcal{E}[Q_k],
\end{aligned}$$

provided that

$$\delta t \leq 2/\max\{\overline{D^2\psi}, \overline{D^2\phi}\}, \tag{3.34}$$

as desired. □

The result of Theorem 9 is not so useful because of the additional regularity required on Q_k.

3.3.3. Gradient descent using convex splitting

Another related strategy is *convex-splitting*, which is popular in gradient flow schemes [96, 100, 97]. Let

$$\psi(Q) \equiv \psi_c(Q) - \psi_e(Q), \tag{3.35}$$

where ψ_c and ψ_e are convex functions of Q. We modify (3.23) by treating ψ_c implicitly and ψ_e explicitly. We also drop the nonlinear ϕ term so that

$$\mathcal{E}[Q] = \frac{1}{2} a\left(Q, Q\right) + \frac{1}{\eta^2}\left(\psi(Q), 1\right)_\Omega - l_{\mathrm{rhs}}(Q), \tag{3.36}$$

and simplify the definition of the time stepping inner product to $(P, T)_{\delta t} := (P, T)_\Omega$. Then, (3.26) is replaced by the following. Given Q_k, find $Q_{k+1} \in \mathbf{V}$ such that

$$\begin{aligned} &\delta t^{-1}\left(Q_{k+1} - Q_k, P\right)_{\delta t} + a\left(Q_{k+1}, P\right) + \left(1/\eta^2\right)\left(D\psi_c(Q_{k+1}), P\right)_\Omega \\ &= l_{\mathrm{rhs}}(P) + \left(1/\eta^2\right)\left(D\psi_e(Q_k), P\right)_\Omega, \quad \forall P \in \mathbf{V}. \end{aligned} \tag{3.37}$$

This scheme also has an energy decrease property with a time-step restriction, for which the following lemma is needed.

Lemma 10. *Let $Q, P \in \mathbf{S}_0$ be any tensors. Then*

$$\psi(P) - \psi(T) \leq \left(D\psi_c(P) - D\psi_e(T)\right) : (P - T). \tag{3.38}$$

Proof. We first invoke the Fundamental Theorem of Calculus, and then evaluate the resulting inner derivative using the chain rule:

$$\psi(P) - \psi(T) = \int_0^1 \frac{d}{d\theta}\left[\psi(S_\theta)\right] d\theta = \int_0^1 D\psi(S_\theta) : (P - T)\, d\theta,$$

where $S_\theta := T + \theta(P - T)$. With a bit of algebra this may be rewritten so that

$$\psi(P) - \psi(T) = (D\psi_c(P) - D\psi_e(T)) : (P - T) + \int_0^1 \xi(\theta)\, d\theta,$$

where

$$\xi(\theta) := \underbrace{(D\psi_c(S_\theta) - D\psi_c(P)) : (P - T)}_{=:\xi_1(\theta)} + \underbrace{(D\psi_e(S_\theta) - D\psi_e(T)) : (T - P)}_{=:\xi_2(\theta)}.$$

What remains is to show that $\xi(\theta) \leq 0$ for all $\theta \in [0, 1]$. We can do this by showing that the first and second terms of ξ are bounded above by 0. For the first term, note that

$$\frac{d}{d\theta}\big[(D\psi_c(S_\theta) - D\psi_c(P)) : (P - T)\big] = (P - T) : D^2\psi_c(S_\theta)(P - T) \geq 0,$$

since $D^2\psi_c(S_\theta)$ is positive definite. And so ξ_1 is monotonically increasing with respect to θ. Thus, for all $\theta \in [0, 1]$, we have

$$(D\psi_c(S_\theta) - D\psi_c(P)) : (P - T) \leq (D\psi_c(S_1) - D\psi_c(P)) : (P - T) = 0,$$

which shows that the first term is bounded above by 0.

For the second term, we have

$$\frac{d}{d\theta}\big[(D\psi_e(S_\theta) - D\psi_e(T)) : (T - P)\big] = -(P - T) : D^2\psi_e(S_\theta)(P - T) \leq 0,$$

since $D^2\psi_e(S_\theta)$ is positive definite. Thus, ξ_2 is monotonically decreasing with respect to θ. And so, for all $\theta \in [0, 1]$, we have

$$(D\psi_e(S_\theta) - D\psi_e(P)) : (T - P) \leq (D\psi_e(S_0) - D\psi_e(P)) : (T - P) = 0,$$

which shows the second term is also bounded above by 0, as desired. □

Theorem 11. *The sequence* $\{Q_k\}_{k=0}^{\infty}$ *defined by the method in* (3.37) *is monotonically energy decreasing, i.e.*

$$\mathcal{E}[Q_{k+1}] \leq \mathcal{E}[Q_k],$$

provided that

$$\delta t \leq \frac{2\alpha_1}{108\ell_1^2\tau_0^2 - \alpha_1^2}, \tag{3.39}$$

where α_1 *is the coercivity constant in* (3.5)*. If* $|\tau_0| \leq \alpha_1/(2\sqrt{27}\ell_1)$*, there is no restriction on* δt*.*

Proof. The first series of inequalities we will prove will bound the difference of energies by integrals of $Q_{k+1} - Q_k$ and its first-order derivatives. First of all, note that since $a(\cdot,\cdot)$ is a bilinear form, we have for all tensors $P, T \in \mathbb{R}^{3\times 3}$ that

$$a\left(P,P\right) - a\left(T,T\right) = -a\left(P-T,P-T\right) + 2a\left(P-T,P\right).$$

In particular, letting $S_{k+1} := Q_{k+1} - Q_k$,

$$a\left(Q_{k+1},Q_{k+1}\right) - a\left(Q_k,Q_k\right) = -a\left(S_{k+1},S_{k+1}\right) + 2a\left(S_{k+1},Q_{k+1}\right). \tag{3.40}$$

We can also substitute $P = S_{k+1}$ into (3.37), as in the proofs for the implicit-explicit and fully implicit cases, and arrive at

$$\begin{aligned} -\delta t^{-1}\left(S_{k+1},S_{k+1}\right)_{\delta t} &= a\left(Q_{k+1},S_{k+1}\right) \\ &\quad + \left(1/\eta^2\right)\left(D\psi_c(Q_{k+1}) - D\psi_e(Q_k), S_{k+1}\right)_{\Omega} - l_{\mathrm{rhs}}(S_{k+1}). \end{aligned} \tag{3.41}$$

Thus we obtain from (3.36) combined with (3.38), (3.40), and (3.41):

$$\begin{aligned}\mathcal{E}[Q_{k+1}] - \mathcal{E}[Q_k] &= (1/2)a\left(Q_{k+1}, Q_{k+1}\right) - (1/2)a\left(Q_k, Q_k\right) \\ &\quad + (1/\eta^2)\left(\psi(Q_{k+1}) - \psi(Q_k), 1\right)_\Omega - l_{\mathrm{rhs}}(S_{k+1}) \\ &\leq (-1/2)a\left(S_{k+1}, S_{k+1}\right) + a\left(S_{k+1}, Q_{k+1}\right) \\ &\quad + (1/\eta^2)\left(D\psi_c(Q_{k+1}) - D\psi_e(Q_k), S_{k+1}\right)_\Omega - l_{\mathrm{rhs}}(S_{k+1}) \\ &= -(1/2)a\left(S_{k+1}, S_{k+1}\right) - \delta t^{-1}\left(S_{k+1}, S_{k+1}\right)_{\delta t}.\end{aligned}$$

Now, we rewrite the form $a\left(\cdot,\cdot\right)$ using (3.9), then bound it using (3.5), the estimate in (3.8), as well as a weighted Young's inequality:

$$\begin{aligned}-(1/2)a\left(S_{k+1}, S_{k+1}\right) &= -(1/2)a_{\mathrm{e}}\left(S_{k+1}, S_{k+1}\right) - (1/2)a_{\mathrm{t}}\left(S_{k+1}, S_{k+1}\right) \\ &\quad - (1/2)a_{\mathrm{s}}\left(S_{k+1}, S_{k+1}\right) \\ &\leq -\frac{\alpha_1}{2}\|S_{k+1}\|_{1,\Omega}^2 + 2\sqrt{27}\ell_1\tau_0\|\nabla S_{k+1}\|_{0,\Omega}\|S_{k+1}\|_{0,\Omega} \\ &\leq \frac{1}{2}\left(c\delta - \alpha_1\right)\|\nabla S_{k+1}\|_{0,\Omega}^2 + \frac{1}{2}\left(\frac{c}{\delta} - \alpha_1\right)\|S_{k+1}\|_{0,\Omega}^2,\end{aligned}$$

where $c = 2\sqrt{27}\ell_1\tau_0$ and $\delta > 0$. Choosing $\delta = \alpha_1/c$, we get

$$-(1/2)a\left(S_{k+1}, S_{k+1}\right) \leq \left(\frac{c^2}{2\alpha_1} - \frac{\alpha_1}{2}\right)\|S_{k+1}\|_{0,\Omega}^2.$$

Thus, combining this with the above, we obtain

$$\mathcal{E}[Q_{k+1}] - \mathcal{E}[Q_k] \leq \left(\frac{c^2}{2\alpha_1} - \frac{\alpha_1}{2} - \frac{1}{\delta t}\right)\|S_{k+1}\|_{0,\Omega}^2 \leq 0,$$

provided that

$$\delta t \leq \frac{2\alpha_1}{(4 \cdot 27\ell_1^2\tau_0^2) - \alpha_1^2}.$$

The above also implies that if $|\tau_0| \leq \alpha_1/(2\sqrt{27}\ell_1)$, there is no restriction on the size of δt. □

Usually, a convex splitting scheme is used to *avoid* a time-step restriction. However, the above discussion shows that a sufficiently large τ_0 will cause a restriction. Moreover, according to [97], a convex splitting scheme is nothing but a fully implicit scheme with time re-scaled (when $\tau_0 = 0$). Thus, we always use the fully implicit scheme as our gradient descent strategy to find a minimizer of $\mathcal{E}[\cdot]$.

Chapter 4. Finite Element Method

We approximate (3.26) by a finite element method [21]. In doing so, we assume that $\Omega \subset \mathbb{R}^3$ is discretized by a conforming shape regular triangulation $\mathcal{T}_h = \{T_i\}$ consisting of tetrahedra, i.e. we define $\Omega_h := \cup_{T\in\mathcal{T}_h} T$, where h is the maximum diameter of the elements in $\mathcal{T}_h$. For the sake of simplicity, we assume that Ω is a box-like domain, or polyhedral, so that $\Omega_h = \Omega$. One can consider curved domains as well and derive error estimates using the theory developed in [62].

Let $\mathbb{M}_h(\Omega_h)$ be the space of continuous, piecewise Lagrange polynomial functions on Ω_h, subordinate to the mesh $\mathcal{T}_h$ of Ω_h, with polynomial degree r, i.e.:

$$\mathbb{M}_h(\Omega_h) := \left\{ v \in C^0(\Omega_h) \mid v|_T \in \mathcal{P}_r(T),\ \forall T \in \mathcal{T}_h \right\}, \tag{4.1}$$

where $\mathcal{P}_r(T)$ is the space of all polynomials of degree $\leq r$ on T, with $r \geq 1$.

In Section 4.2, we present a numerical analysis for the discretization of the *equilibrium* problem, i.e. we derive an error estimate (Theorem 13) for the finite element approximation of a (local) minimizer of (2.18). In particular, we will show that a minimum mesh size is required to obtain an error estimate because of the non-convexity of the double-well potential and cholesteric twist term.

4.1. Discretization of the Cholesteric Landau-de Gennes Model

We discretize (3.26) by approximating Q by a finite element function Q_h. To this end, define

$$\mathbb{S}_h(\Omega_h) := \left\{ P \in C^0(\Omega_h; \mathbf{S}_0) \mid P = q_{i,h} E^i,\ q_{i,h} \in \mathbb{M}_h(\Omega_h), 1 \leq i \leq 5 \right\}, \tag{4.2}$$

and let $Q_h \in \mathbf{V}_h := \mathbb{S}_h(\Omega_h) \subset \mathbf{V}$. Thus, $Q_h = q_{i,h} E^i$, and $q_{i,h} \in H^1(\Omega)$ for $i = 1, \ldots, 5$.

The fully discrete L^2-gradient flow now follows from (3.26), i.e. given $Q_{h,k}$, find $Q_{h,k+1} \in \mathbf{V}_h$ such that

$$\delta t^{-1} \left(Q_{h,k+1} - Q_{h,k}, P_h\right)_{\delta t} = -\delta_Q \mathcal{E}[Q_{h,k+1}; P_h], \quad \forall P_h \in \mathbf{V}_h, \tag{4.3}$$

We iterate this procedure until some stopping criteria is achieved (see Section 5.1). Since $\mathbf{V}_h \subset \mathbf{V}$, the same arguments in Section 3.3 still hold when replacing $\mathbf{V}$ by $\mathbf{V}_h$. Therefore, the same time-stepping restrictions apply to the fully discrete formulation.

4.2. Numerical Analysis for the Equilibrium Problem

4.2.1. Preliminary Facts and Assumptions

We seek to derive an error estimate for a local minimizer of the LdG energy, which has the form

$$\mathcal{E}[Q] = (1/2)a\left(Q, Q\right) + (1/\eta^2)\left(\psi(Q), 1\right)_\Omega + (1/\omega)\left(\phi(Q), 1\right)_\Gamma - l_{\text{rhs}}(Q). \tag{4.4}$$

If $Q \in \mathbf{V}$ is a local minimizer of $\mathcal{E}[\cdot]$, then

$$\begin{aligned} \delta\mathcal{E}[Q](P) = a\left(Q, P\right) + (1/\eta^2)\left(D\psi(Q), P\right)_\Omega \\ + (1/\omega)\left(D\phi(Q), P\right)_\Gamma - l_{\text{rhs}}(P) = 0, \quad \forall P \in \mathbf{V}. \end{aligned} \tag{4.5}$$

Moreover, let $Q_h \in \mathbf{V}_h$ be a local minimizer of $\mathcal{E}[\cdot]$; thus,

$$\begin{aligned} \delta\mathcal{E}[Q_h](P_h) = a\left(Q_h, P_h\right) + (1/\eta^2)\left(D\psi(Q_h), P_h\right)_\Omega \\ + (1/\omega)\left(D\phi(Q_h), P_h\right)_\Gamma - l_{\text{rhs}}(P_h) = 0, \quad \forall P_h \in \mathbf{V}_h. \end{aligned} \tag{4.6}$$

In order to derive an error estimate, we need the following assumption, which says that the energy landscape around a minimizer is not too flat.

Assumption 12 (Isolated minimizer and coercivity)**.** *For a given local minimizer Q of $\mathcal{E}$, we assume there exists $\zeta > 0$ such that for all $\tilde{Q}$ with $\|Q - \tilde{Q}\|_{1,\Omega} < \zeta$, the following two*

inequalities hold:

$$\mathcal{E}[Q] \leq \mathcal{E}[\tilde{Q}], \tag{4.7}$$

$$\begin{aligned} \delta^2\mathcal{E}[\tilde{Q}](P,P) = a\,(P,P) + (1/\eta^2)\left(P, D^2\psi(\tilde{Q})P\right)_\Omega \\ +(1/\omega)\left(P, D^2\phi(\tilde{Q})P\right)_\Gamma \geq m_0\|P\|^2_{1,\Omega}, \end{aligned} \tag{4.8}$$

for some $m_0 > 0$ *and all* $P \in \mathbf{V}$.

4.2.2. Error Estimates

In order to avoid additional technicalities, and streamline the presentation, we assume that if Q is a solution of (4.5), then it has the additional regularity $Q \in H^2(\Omega)$. Moreover, we also assume an associated adjoint problem also enjoys additional $H^2(\Omega)$ regularity; see Remark 17 for further details. We have the following result that yields an error estimate for the finite element solution Q_h, which requires a *restriction* on the mesh size h.

Theorem 13. *Let* $Q \in \mathbf{V}$ *be a local minimizer of* $\mathcal{E}[\cdot]$ *that satisfies* (3.1) *and also satisfies* $Q \in H^2(\Omega)$, *and let* $Q_h \in \mathbf{V}_h$ *be a local minimizer of* $\mathcal{E}[\cdot]$ *that satisfies* (4.6). *Moreover, adopt Assumption 12 and assume that* $\|Q - Q_h\|_{1,\Omega} < \zeta$. *Then, there exists* $c > 0$ *such that for all* $h \leq h_0$, *we have* $\|Q - Q_h\|_{1,\Omega} \leq ch|Q|_{2,\Omega}$, *where*

$$h_0 = \left(\frac{\alpha_1}{k + (a'/\eta^2) + (s''/\omega^2)}\right)^{1/2} \frac{1}{\sqrt{8}(c_0 + \beta_1'/\eta^2 + \beta_2'/\omega)c_2c_3}, \tag{4.9}$$

where $k = \max\left((216\ell_1^2\tau_0^2/\alpha_1) - (\alpha_1/2), 0\right)$, c_1, c_2, c_3, β_1', β_2', a', *and* s'' *are constants depending on the domain, and*

$$c_0 = \ell_1 + 3\ell_2 + \ell_3 + 4\ell_1\sqrt{27}\tau_0 + \beta_3(w_0 + 3w_1) \tag{4.10}$$

is the constant such that $|a\,(Q,P)\,| \leq c_0\|Q\|_{1,\Omega}\|P\|_{1,\Omega}$, *with* β_3 *also depending on the domain.*

Note that (4.9) says that small values of η and ω, and large values of τ_0, lead to small values of h_0. Furthermore, Theorem 13 says there is *no* error estimate if the mesh size is too large. This means that the discrete problem may have *no* connection to the physical problem of interest.

To facilitate the proof of Theorem 13, we first give several intermediate results.

Lemma 14 (Gårding's inequality)**.** *There exists $k \geq 0$ such that*

$$a\left(P,P\right)+k\|P\|_{0,\Omega}^{2} \geq \frac{\alpha_1}{2}\|P\|_{1,\Omega}^{2}, \qquad \forall P \in \mathbf{V},$$

where α_1 is the constant found in (3.5)*.*

Proof. We follow the proof found in [21], with modifications for our particular case. First, note the coercivity result from (3.5): $a_{\mathrm{e}}\left(P,P\right)+a_{\mathrm{s}}\left(P,P\right) \geq \alpha_1\|P\|_{1,\Omega}^{2}$. Next, recall (3.9) and note that $|\varepsilon_{ikl}\left(P_{jk,l},P_{ij}\right)_{\Omega}| \leq \sqrt{27}|P|_{1,\Omega}\|P\|_{0,\Omega}$, and using a weighted Young's inequality, we have

$$\begin{aligned}
a\left(P,P\right)+k\|P\|_{0,\Omega}^{2} &\geq \alpha_1\|P\|_{1,\Omega}^{2}+4\ell_1\tau_0\varepsilon_{ikl}\left(P_{jk,l},P_{ij}\right)_{\Omega}+k\|P\|_{0,\Omega}^{2} \\
&\geq \alpha_1\|P\|_{1,\Omega}^{2}-(4\ell_1\sqrt{27})\tau_0|P|_{1,\Omega}\|P\|_{0,\Omega}+k\|P\|_{0,\Omega}^{2} \\
&\geq \alpha_1|P|_{1,\Omega}^{2}-2\ell_1\sqrt{27}\tau_0\delta|P|_{1,\Omega}^{2}-2\ell_1\sqrt{27}\tau_0\delta^{-1}\|P\|_{0,\Omega}^{2}+(k+\alpha_1)\|P\|_{0,\Omega}^{2} \\
&= \left(\alpha_1-2\ell_1\sqrt{27}\tau_0\delta\right)|P|_{1,\Omega}^{2}+\left(k+\alpha_1-2\ell_1\sqrt{27}\tau_0\delta^{-1}\right)\|P\|_{0,\Omega}^{2} \\
&\geq (\alpha_1/2)\|\nabla P\|_{0,\Omega}^{2}+(\alpha_1/2)\|P\|_{0,\Omega}^{2}.
\end{aligned}$$

Finally, by choosing $\delta=\alpha_1/(4\ell_1\tau_0\sqrt{27})$ the result follows by assuming

$$k=\max\left[\left(\frac{216\ell_1^{2}\tau_0^{2}}{\alpha_1}-\frac{\alpha_1}{2}\right),0\right]. \tag{4.11}$$

Thus the proof is complete. □

Lemma 15. *The following inequality holds:*

$$\frac{\alpha_1}{4}\|Q-Q_h\|_{1,\Omega}^2 \le c_1\|Q-Q_h\|_{1,\Omega}\|Q-P_h\|_{1,\Omega} + \tilde{k}\|Q-Q_h\|_{0,\Omega}^2, \qquad \forall P_h \in \mathbf{V}_h,$$

where c_1 and $\tilde{k}$ are nonnegative constants, and Q, Q_h are defined in Thm. 13.

Proof. First, observe that, by subtracting (4.6) from (3.18) (choosing $P = P_h \in \mathbf{V}_h$), we obtain

$$a\left(Q-Q_h, P_h\right) + (1/\eta^2)\left(D\psi(Q) - D\psi(Q_h), P_h\right)_\Omega + (1/\omega)\left(D\phi(Q) - D\phi(Q_h), P_h\right)_\Gamma = 0, \tag{4.12}$$

for all $P_h \in \mathbf{V}_h$. Secondly, for all symmetric tensors Q_1, Q_2, P, note that:

$$\begin{aligned}
(D\psi(Q_1) - D\psi(Q_2)) : P &= -a_2(H:P) - a_3(Q_1^2 - Q_2^2) : P + a_4(|Q_1|^2Q_1 - |Q_2|^2Q_2) : P \\
&= -a_2(H:P) - a_3(H:(Q_1+Q_2)P) \\
&\quad + \frac{a_4}{2}\Big[(|Q_1|^2+|Q_2|^2)H : P + (H:(Q_1+Q_2))((Q_1+Q_2):P)\Big] \\
&= H : \bigg(- a_2\mathcal{I} - a_3(Q_1+Q_2)\mathcal{I} + \frac{a_4}{2}\Big[(|Q_1|^2+|Q_2|^2)\mathcal{I} \\
&\qquad + (Q_1+Q_2)\otimes(Q_1+Q_2)\Big]\bigg)P =: H : \Theta(Q_1,Q_2)P,
\end{aligned}$$

where $H = Q_1 - Q_2$ and $\mathcal{I}$ is the 4-tensor identity. Similarly, we have

$$\begin{aligned}
(D\phi(Q_1) - D\phi(Q_2)) : P &= -\frac{2s_0}{3}H : P + (|Q_1|^2Q_1 - |Q_2|^2Q_2) : P \\
&= -\frac{2s_0^2}{3}H : P + (1/2)\Big[(|Q_1|^2+|Q_2|^2)H : P + (P:(Q_1+Q_2))((Q_1+Q_2):H)\Big] \\
&= H : \bigg(- \frac{2s_0^2}{3}\mathcal{I} + (1/2)\Big[(|Q_1|^2+|Q_2|^2)\mathcal{I} \\
&\qquad + (Q_1+Q_2)\otimes(Q_1+Q_2)\Big]\bigg)P =: H : \Xi(Q_1,Q_2)P.
\end{aligned}$$

Note also that these tensors obey the inequality

$$\begin{aligned}(P,\Theta(Q_1,Q_2)P)_\Omega &\geq \int_\Omega -a_2|P|^2 - a_3(P:(Q_1+Q_2)P) + (a_4/2)(|Q_1|^2+|Q_2|^2)|P|^2 \\ &\geq \int_\Omega -a_2|P|^2 - (a_3\delta^{-1}/2)|P|^2 - (a_3\delta/2)|Q_1+Q_2|^2|P|^2 \\ &\qquad + (a_4/2)(|Q_1|^2+|Q_2|^2)|P|^2 \\ &\geq \int_\Omega -a_2|P|^2 - (a_3\delta^{-1}/2)|P|^2 - (a_3\delta)(|Q_1|^2+|Q_2|^2)|P|^2 \\ &\qquad + (a_4/2)(|Q_1|^2+|Q_2|^2)|P|^2 \\ &= -(a_2+a_3^2/a_4)\|P\|_{0,\Omega}^2 = -a'\|P\|_{0,\Omega}^2,\end{aligned}$$

and also

$$\begin{aligned}(P,\Xi(Q_1,Q_2)P)_\Gamma &= \int_\Gamma -(2s_0^2/3)|P|^2 + (1/2)(|Q_1|^2+|Q_2|^2)|P|^2 + (1/2)((Q_1+Q_2):P)^2 \\ &\geq \int_\Gamma -(2s_0^2/3)|P|^2 = -s'\|P\|_{0,\Gamma}^2,\end{aligned}$$

for all Q_1, Q_2, P, where we have chosen $\delta = a_4/2a_3$, $a' = a_2 + a_3^2/a_4$, and $s' = 2s_0^2/3$. Then, for all $P_h \in \mathbf{V}_h$, we have

$$\begin{aligned}a\left(Q-Q_h, Q-Q_h\right) &= a\left(Q-Q_h, Q-P_h\right) + a\left(Q-Q_h, P_h-Q_h\right) \\ &= a\left(Q-Q_h, Q-P_h\right) - (1/\eta^2)\left(D\psi(Q)-D\psi(Q_h), P_h-Q_h\right)_\Omega \\ &\qquad - (1/\omega)\left(D\phi(Q)-D\phi(Q_h), P_h-Q_h\right)_\Omega.\end{aligned}$$

Substituting Θ and Ξ into the above, we see that

$$\begin{aligned}
a\left(Q-Q_h, Q-Q_h\right) &= a\left(Q-Q_h, Q-P_h\right) - \left(1/\eta^2\right)\left(Q-Q_h, \Theta(Q,Q_h)(P_h-Q_h)\right)_\Omega \\
&\quad - \left(1/\omega\right)\left(Q-Q_h, \Xi(Q,Q_h)(P_h-Q_h)\right)_\Gamma \\
&= a\left(Q-Q_h, Q-P_h\right) + \left(1/\eta^2\right)\left(Q-Q_h, \Theta(Q,Q_h)(Q-P_h)\right)_\Omega \\
&\quad + \left(1/\omega\right)\left(Q-Q_h, \Xi(Q,Q_h)(Q-P_h)\right)_\Gamma \\
&\quad -\left(1/\eta^2\right)\left(Q-Q_h, \Theta(Q,Q_h)(Q-Q_h)\right)_\Omega - \left(1/\omega\right)\left(Q-Q_h, \Xi(Q,Q_h)(Q-Q_h)\right)_\Gamma \\
&\leq c_0\|Q-Q_h\|_{1,\Omega}\|Q-P_h\|_{1,\Omega} \\
&\quad + (1/\eta^2)\|\Theta(Q,Q_h)\|_{0,3,\Omega}\|Q-Q_h\|_{0,6,\Omega}\|Q-P_h\|_{0,\Omega} \\
&\quad + (1/\omega)\|\Xi(Q,Q_h)\|_{0,\Gamma}\|Q-Q_h\|_{0,4,\Gamma}\|Q-P_h\|_{0,4,\Gamma} \\
&\quad + \frac{a'}{\eta^2}\|Q-Q_h\|_{0,\Omega}^2 + \frac{s'}{\omega}\|Q-Q_h\|_{0,\Gamma}^2,
\end{aligned}$$

where c_0 is the continuity constant defined in (4.10). Applying the Sobolev trace and embedding theorems, with induced constants $\beta_1, \beta_2 > 0$, we get

$$\begin{aligned}
a\left(Q-Q_h, Q-Q_h\right) &\leq c_0\|Q-Q_h\|_{1,\Omega}\|Q-P_h\|_{1,\Omega} \\
&\quad + (\beta_1/\eta^2)\|\Theta(Q,Q_h)\|_{0,3,\Omega}\|Q-Q_h\|_{1,\Omega}\|Q-P_h\|_{1,\Omega} \\
&\quad + (\beta_2/\omega)\|\Xi(Q,Q_h)\|_{0,\Gamma}\|Q-Q_h\|_{1,\Omega}\|Q-P_h\|_{1,\Omega} \\
&\quad + \frac{a'}{\eta^2}\|Q-Q_h\|_{0,\Omega}^2 + \frac{s'}{\omega}\|Q-Q_h\|_{0,\Gamma}^2.
\end{aligned}$$

Next, by another classic trace theorem, $\|P\|_{0,\Gamma}^2 \leq \beta_3\|P\|_{0,\Omega}\|P\|_{1,\Omega}$ combined with a weighted inequality, we have

$$\frac{s'}{\omega}\|Q-Q_h\|_{0,\Gamma}^2 \leq \frac{\left(\beta_3 s'\right)^2}{\omega^2\alpha_1}\|Q-Q_h\|_{0,\Omega}^2 + \frac{\alpha_1}{4}\|Q-Q_h\|_{1,\Omega}^2,$$

which leads to

$$a\left(Q-Q_h, Q-Q_h\right) \leq c_1 \|Q-Q_h\|_{1,\Omega}\|Q-P_h\|_{1,\Omega} + \left(\frac{a'}{\eta^2} + \frac{\left(\beta_3 s'\right)^2}{\omega^2 \alpha_1}\right)\|Q-Q_h\|_{0,\Omega}^2 + \frac{\alpha_1}{4}\|Q-Q_h\|_{1,\Omega}^2,$$

where

$$c_1 := c_0 + (\beta_1/\eta^2)\|\Theta(Q,Q_h)\|_{0,3,\Omega} + (\beta_2/\omega)\|\Xi(Q,Q_h)\|_{0,\Gamma} = c_0 + \beta_1'/\eta^2 + \beta_2'/\omega. \tag{4.13}$$

Now, by Gårding's inequality, we have

$$\frac{\alpha_1}{2}\|Q-Q_h\|_{1,\Omega}^2 \leq a\left(Q-Q_h, Q-Q_h\right) + k\|Q-Q_h\|_{0,\Omega}^2.$$

And so, if we combine this with the above, define $s'' = \left(\beta_3 s'\right)^2/\alpha_1$, and set

$$\tilde{k} = k + \frac{a'}{\eta^2} + \frac{s''}{\omega^2}, \tag{4.14}$$

then the proof is complete. □

Now we move towards an estimate in $L^2(\Omega)$ of $Q - Q_h$. In order to do this, we first introduce the solution to and regularity of an adjoint problem.

Lemma 16. *There exists a solution $R \in \mathbf{V}$ to the adjoint problem*

$$a\left(P,R\right) + \left(1/\eta^2\right)\left(R, \Theta(Q,Q_h)P\right)_\Omega + \left(1/\omega\right)\left(R, \Xi(Q,Q_h)P\right)_\Gamma = \left(Q-Q_h, P\right)_\Omega, \qquad \forall P \in \mathbf{V}, \tag{4.15}$$

where we assume the regularity estimate

$$|R|_{2,\Omega} \leq c_3\|Q-Q_h\|_{0,\Omega}. \tag{4.16}$$

Proof. First note the inequality

$$\begin{aligned} P : \Theta(Q, Q_h)P &= -a_2|P|^2 - a_3(P : (Q_1 + Q_2)P) + (a_4/2)\bigg((|Q_1|^2 + |Q_2|^2)|P|^2 \\ &\qquad + (P : (Q_1 + Q_2))^2\bigg) \\ &= -a_2|P|^2 - 2a_3(P : \bar{Q}P) + a_4\bigg(\frac{|Q_1|^2 + |Q_2|^2}{2}|P|^2 + 2(\bar{Q} : P)^2\bigg) \\ &\geq -a_2|P|^2 - 2a_3(P : \bar{Q}P) + a_4\bigg(|\bar{Q}|^2|P|^2 + 2(\bar{Q} : P)^2\bigg) = P : D^2\psi(\bar{Q})P, \end{aligned}$$

as well as the inequality,

$$\begin{aligned} P : \Xi(Q, Q_h)P &= -(2s_0^2/3)|P|^2 + (1/2)\bigg((|Q_1|^2 + |Q_2|^2)|P|^2 + (P : (Q_1 + Q_2))^2\bigg) \\ &\geq -(2s_0^2/3)|P|^2 + \bigg(|\bar{Q}|^2|P|^2 + 2(\bar{Q} : P)^2\bigg) = P : D^2\phi(\bar{Q})P, \end{aligned}$$

where $\bar{Q} = (Q_1 + Q_2)/2$, and where we have used the Cauchy-Schwarz and Young inequalities. From here, using (4.8), we see that

$$\begin{aligned} &a\,(P, P) + (1/\eta^2)\,(P, \Theta(Q, Q_h)P)_\Omega + (1/\omega)\,(P, \Xi(Q, Q_h)P)_\Gamma \\ &\qquad \geq a\,(P, P) + (1/\eta^2)\left(P, D^2\psi(\bar{Q})P\right)_\Omega + \left(P, D^2\phi(\bar{Q})P\right)_\Gamma \geq m_0\|P\|_{1,\Omega}^2, \end{aligned}$$

showing that this problem is coercive, and so the solution to the above is guaranteed by Lax-Milgram, which also shows that $\|R\|_{1,\Omega} \leq c\|Q - Q_h\|_{0,\Omega}$ for some constant $c > 0$. □

Remark 17. *The additional $H^2(\Omega)$ regularity assumed in Thm. 13 on the solution Q, as well as the additional regularity on the adjoint solution in* (4.16)*, may be shown rigorously (given certain smoothness assumptions on Ω) by applying bootstrapping techniques, and combining the previous a priori estimate for $\|R\|_{1,\Omega}$ with the theory in [45, Ch. 4]. See [38, 43] for other techniques for proving higher regularity of solutions to elliptic* systems.

Lemma 18. *The following estimate holds for the L^2-norm difference of Q and its finite element approximation:*

$$\|Q - Q_h\|_{0,\Omega} \leq c_4 h \|Q - Q_h\|_{1,\Omega}.$$

Proof. Starting from (4.12), replace P_h with $R_h \in \mathbf{V}_h$ and use Θ and Ξ from earlier to get:

$$a\left(Q - Q_h, R_h\right) + (1/\eta^2)\left(R_h, \Theta(Q, Q_h)(Q - Q_h)\right)_\Omega + (1/\omega)\left(R_h, \Xi(Q, Q_h)(Q - Q_h)\right)_\Gamma = 0.$$

Then, set $P = Q - Q_h$ in (4.15) to produce an estimate for $\|Q - Q_h\|_{0,\Omega}$:

$$\begin{aligned}
(Q - Q_h, Q - Q_h)_\Omega &= a\left(Q - Q_h, R\right) + (1/\eta^2)\left(R, \Theta(Q, Q_h)(Q - Q_h)\right)_\Omega \\
&\quad + (1/\omega)\left(R, \Xi(Q, Q_h)(Q - Q_h)\right)_\Gamma \\
&= a\left(Q - Q_h, R - R_h\right) + (1/\eta^2)\left(R - R_h, \Theta(Q, Q_h)(Q - Q_h)\right)_\Omega \\
&\quad + (1/\omega)\left(R - R_h, \Xi(Q, Q_h)(Q - Q_h)\right)_\Gamma \\
&\leq a\left(Q - Q_h, R - R_h\right) \\
&\quad + (1/\eta^2)\|\Theta(Q, Q_h)\|_{0,3,\Omega}\|R - R_h\|_{0,6,\Omega}\|Q - Q_h\|_{0,\Omega} \\
&\quad + (1/\omega)\|\Xi(Q, Q_h)\|_{0,\Gamma}\|R - R_h\|_{0,4,\Gamma}\|Q - Q_h\|_{0,4,\Gamma}.
\end{aligned}$$

We apply the Sobolev trace and embedding theorems to the above line and obtain that

$$\begin{aligned}
(Q - Q_h, Q - Q_h)_\Omega &\leq a\left(Q - Q_h, R - R_h\right) \\
&\quad + (\beta_1/\eta^2)\|\Theta(Q, Q_h)\|_{0,3,\Omega}\|R - R_h\|_{1,\Omega}\|Q - Q_h\|_{1,\Omega} \\
&\quad + (\beta_2/\omega)\|\Xi(Q, Q_h)\|_{0,\Gamma}\|R - R_h\|_{1,\Omega}\|Q - Q_h\|_{1,\Omega} \\
&\leq c_0\|Q - Q_h\|_{1,\Omega}\|R - R_h\|_{1,\Omega} + \big((\beta_1/\eta^2)\|\Theta(Q, Q_h)\|_{0,3,\Omega} \\
&\quad + (\beta_2/\omega)\|\Xi(Q, Q_h)\|_{0,\Gamma}\big)\|Q - Q_h\|_{1,\Omega}\|R - R_h\|_{1,\Omega} \\
&= c_1\|Q - Q_h\|_{1,\Omega}\|R - R_h\|_{1,\Omega},
\end{aligned}$$

for all $R_h \in \mathbf{V}_h$, where $\beta_1, \beta_2 > 0$ are constants induced from the trace and embedding theorems, and c_1 is the same as in (4.13). We then note that $\inf_{P_h \in \mathbf{V}_h} \|P - P_h\|_{1,\Omega} \leq c_2 h |P|_{2,\Omega}$ for all $P \in H^2(\Omega)$, for some constant $c_2 > 0$, a result from standard finite element interpolation theory (cf. [21], for instance). So, we can choose R_h such that by this estimate as well as (4.16), we obtain

$$(Q - Q_h, Q - Q_h)_\Omega \leq c_1 c_2 h \|Q - Q_h\|_{1,\Omega} |R|_{2,\Omega} \leq c_1 c_2 c_3 h \|Q - Q_h\|_{1,\Omega} \|Q - Q_h\|_{0,\Omega}.$$

Dividing everything by $\|Q - Q_h\|_{0,\Omega}$, we obtain

$$\|Q - Q_h\|_{0,\Omega} \leq c_4 h \|Q - Q_h\|_{1,\Omega}, \tag{4.17}$$

where $c_4 := c_1 c_2 c_3$ and we are done. □

Proof of Theorem 13. Combining Lemma 15 with Lemma 18, we obtain the following for all $P_h \in \mathbf{V}_h$:

$$\begin{aligned} \text{Lem. 15}: \quad \frac{\alpha_1}{4} \|Q - Q_h\|_{1,\Omega}^2 &\leq c_1 \|Q - Q_h\|_{1,\Omega} \|Q - P_h\|_{1,\Omega} + \tilde{k} \|Q - Q_h\|_{0,\Omega}^2 \\ &\leq c_1 \|Q - Q_h\|_{1,\Omega} \|Q - P_h\|_{1,\Omega} + \tilde{k} (c_1 c_2 c_3)^2 h^2 \|Q - Q_h\|_{1,\Omega}^2. \end{aligned}$$

Moving the last term to the left hand side and then dividing by $\|Q - Q_h\|_{1,\Omega}$:

$$(\alpha_1/4 - \tilde{k}(c_1 c_2 c_3)^2 h^2) \|Q - Q_h\|_{1,\Omega} \leq c_1 \|Q - P_h\|_{1,\Omega}.$$

If we choose $h \leq h_0$, where

$$h_0 = \left(\frac{\alpha_1}{8\tilde{k}} \right)^{1/2} \frac{1}{c_1 c_2 c_3},$$

then

$$\alpha_1 \|Q - Q_h\|_{1,\Omega} \leq 8 c_1 \|Q - P_h\|_{1,\Omega}, \qquad \forall P_h \in \mathbf{V}_h. \tag{4.18}$$

Next, substituting c_1 from (4.13) and $\tilde{k}$ from (4.14), the explicit form of h_0 is

$$h_0 = \left(\frac{\alpha_1}{k + (a'/\eta^2) + (s''/\omega^2)} \right)^{1/2} \frac{1}{\sqrt{8}(c_0 + \beta_1'/\eta^2 + \beta_2'/\omega)c_2 c_3}.$$

Finally, using the interpolation theory result from the previous lemma, we see that the estimate (4.18) is bounded by a multiple of $h|Q|_{2,\Omega}$, thus completing the proof. □

4.3. Numerical Analysis for the Gradient Flow Problem

The previous sections describe the energy decrease property of our gradient flow scheme which is necessary to obtain a local minimizer; this holds for both the continuous problem and the finite element discretized problem. Furthermore, we have shown that a local minimizer for the finite element discretization of the equilibrium problem converges to a local minimizer of the full equilibrium problem as the mesh size h goes to 0, which required Assumption 12 (i.e. the minimizer is isolated and coercive).

One can also analyze the numerical convergence of the fully discrete scheme toward the solution of the continuous gradient flow problem in space and time on a *finite* time-interval, i.e. does the solution of (4.3) converge to the solution of (3.21) as $\delta t \to 0$ and $h \to 0$? This does indeed hold and can be shown by well-known numerical techniques for parabolic equations; for instance, see [96, 83, 97] in the context of phase-field models. However, in many liquid crystal modeling situations, the equilibrium problem is of primary interest.

In addition, the mesh-size restriction that is in Theorem 13 does not appear in the error analysis for the time-dependent problem on a *finite* time-interval. This is due to the fact that the discrete time-derivative term acts to regularize the problem for sufficiently small time-steps. Hence, it can be misleading to only consider the numerical analysis of

the time-dependent problem with respect to the numerical parameters needed to accurately capture the phenomena being modeled. In other words, if the mesh size is not sufficiently small, then the numerical solution of the equilibrium problem may not be trustworthy. Section 5.5 gives examples that demonstrate this.

Chapter 5. Numerical Results

We present several simulations that illustrate the cholesteric Landau-de Gennes model on both a slab geometry and a spherical shell for a range of twist parameters. We illustrate both the richness of the model, as well as issues that can arise when the mesh size is not small enough. Our software is implemented in Firedrake [77], which heavily uses the PETSc library [10, 9, 11], as well as various algorithms for computing and finite elements [50, 64, 52, 51]. We also made use of parallel computing in our simulations [28, 26]. We used Paraview [6] to visualize our simulations. We simulated on two of the machines owned by the LSU Department of Mathematics. Each machine was equipped with two Intel Xeon Gold 6242R processors running at 3.10/4.10 GHz, as well as a 768 GiB RAM. We ran our simulations on a single node using 25 processes.

5.1. Minimization technique

As discussed in Section 3.3, the gradient descent method can be used to find a local minimizer of the LdG equilibrium problem. In our implementation, we apply this method to the finite element discretization of the problem. At each time step, we must solve a nonlinear system in (4.3), so Firedrake's builtin nonlinear solver (which utilizes Newton's method) is employed. We use the Geometric agglomerated Algebraic MultiGrid (GAMG) preconditioner, as well as the Minimal Residual Method (MINRES) for our Krylov subspace method.

However, the fully implicit gradient descent method we use comes with a time-step restriction (see Theorem 8) that is affected by η and ω through the minimizing movements inner product (3.25), as well as the twist τ_0. This can lead to excessive computation times.

Therefore, in practice, we start with a time-step that satisfies the various restrictions given earlier and compute several steps (e.g. we start with a time-step of $\delta t = 0.001$ and we compute 50 steps). Then, we increase the time-step by a factor of 10 and do several more steps (e.g. 50), checking that the energy continues to decrease with each step. If the energy does not decrease after increasing the time-step, or if the solver diverges, then we go back to the smaller time-step and perform more iterations before attempting to increase the time-step again. In practice, however, the energy always decreased in our simulations; the only situation in which we had to go back to the smaller time-step was when the solver diverged. This continues until δt reaches a maximum value of $\delta t = 100,000$, after which we continue iterating. During this procedure, for any value of δt, if the energy decrease between successive iterates is less than a tolerance (e.g. 10^{-6}), then we stop iterating and solve the equilibrium problem directly (i.e. no gradient descent). If the nonlinear solver for the equilibrium problem diverges, then we continue with several more gradient descent iterations. Despite the ad-hoc nature of this procedure, it was effective in obtaining (discrete) local minimizers of the discrete LdG energy in a reasonable amount of time.

5.2. Parameter choices and visualization

The following parameter values were used for all simulations in Sections 5.3, 5.4, and 5.5. The coefficients of the double well in (2.10), were chosen as

$$a_0 = 1, \quad a_2 = 7.502104, \quad a_3 = 60.975813, \quad a_4 = 66.519069. \tag{5.1}$$

The function $\psi(Q)$ has a global minimum at $Q_* = s_0\left(\mathbf{l}\otimes\mathbf{l} - I/3\right)$, where $\mathbf{l} \in \mathbb{R}^3$ is any unit vector, and $s_0 = 0.7$. The other coefficients are given by $\ell_1 = 1.0$, $\ell_2 = \ell_3 = 0$, and $\eta = 0.1$. We conducted experiments with both homeotropic anchoring (i.e. $w_0 = 10.0$,

$w_1 = w_2 = 0$) and planar degenerate anchoring (i.e. $w_0 = 0$, $w_1 = w_2 = 10.0$ and $\omega = 0.1$). The twist was varied, with values typically chosen as $\tau_0 = 0, 5, 10, 15, 20, 25$. In Section 5.6, a different set of parameters was used corresponding to the liquid crystal 5CB.

The numerical solution for Q is visualized by first performing an eigendecomposition of Q at each node of the mesh. We then set $\mathbf{n}$ to be the eigenvector of Q corresponding to the largest eigenvalue of Q. If Q has a uniaxial form, then this choice of $\mathbf{n}$ is consistent with (2.5). Finally, we compute $|\mathbf{n} \cdot \mathbf{r}|$, where $\mathbf{r}$ is a given vector that corresponds to the computational domain, and visualize $|\mathbf{n} \cdot \mathbf{r}|$ as a scalar field. Typically, $\mathbf{r}$ is chosen to face a hypothetical viewer, and this varies depending on the geometry of the LC domain. Thus, $|\mathbf{n} \cdot \mathbf{r}| = 0$ means the LCs are facing orthogonal to the viewer's line of sight, and $|\mathbf{n} \cdot \mathbf{r}| = 1$ means the LCs are facing the viewer directly.

5.3. Slab Configuration

5.3.1. Experimental Setup

The domain Ω is a rectangular solid (slab geometry), where two choices were used with different aspect ratios. For the first slab, we set $\Omega = (0, 1) \times (0, 1) \times (0, 0.2)$. The boundary is partitioned as $\Gamma = \Gamma_1 \cup \Gamma_0$ where $\Gamma_1 = (0, 1) \times (0, 1) \times \{0, 0.2\}$ (top and bottom of the slab) and $\Gamma_0 = \Gamma \setminus \Gamma_1$ (sides of the slab). Then, in the formulation (3.26), we replace Γ with Γ_1, i.e. we enforce the weak anchoring condition on Γ_1 and use a zero Neumann condition on Γ_0. For the finite element discretized domain Ω_h, we chose a mesh size of $h = 0.02$.

The initial condition Q_0 for this case was a periodic function defined as follows.

First, let $\mathbf{w} = \mathbf{w}(x_1, x_2, x_3)$ be given by

$$\mathbf{w} = (0, \cos(\tau_0 x_1), \sin(\tau_0 x_1))^\dagger . \tag{5.2}$$

Then, we set $\mathbf{n} = \mathbf{w}/|\mathbf{w}|$ and

$$Q_0 = s_0 \left(\mathbf{n} \otimes \mathbf{n} - I/3\right). \tag{5.3}$$

This initial condition corresponds to a helical configuration of the director field, which is visualized in the far left column of Figure B.1 where the color corresponds to $|\mathbf{n} \cdot \mathbf{r}|$ with $\mathbf{r} = \mathbf{e}_3$ (see Section 5.2). The period $2\pi/\tau_0$ decreases with larger values of τ_0, which corresponds with more stripes positioned closer together. See Figure B.1 for a visualization of the initial condition Q_0 and the computed local minimizers for both homeotropic and planar degenerate anchoring for a range of twist values τ_0. Note that the color corresponds to $|\mathbf{n} \cdot \mathbf{r}|$ with $\mathbf{r} = \mathbf{e}_3$ (see Section 5.2).

For the larger aspect ratio slab, we set $\Omega = (0, 2) \times (0, 2) \times (0, 0.2)$, with boundary conditions chosen similarly to the smaller slab, i.e. a zero Neumann condition is enforced on the sides of Ω and weak anchoring on the top and bottom. The mesh size was again set to $h = 0.02$. The initial condition was chosen to have an oscillatory component in the following way. First, define

$$\mathbf{w}_1 = (0, \cos(\tau_0 x_1), \sin(\tau_0 x_1))^\dagger, \quad \mathbf{w}_2 = (\cos(\tau_0 x_2), \sin(\tau_0 x_2), 0)^\dagger. \tag{5.4}$$

Then for $i = 1, 2$ we define $\mathbf{n}_i = \mathbf{w}_i/|\mathbf{w}_i|$, and Q_i by

$$Q_i = s_0 \left(\mathbf{n}_i \otimes \mathbf{n}_i - I/3\right). \tag{5.5}$$

Then, choosing $\rho = (\cos(\tau_0 x_1) \cos(\tau_0 x_2) + 1)/2$, we set

$$Q_0 = (1 - \rho) Q_1 + \rho Q_2. \tag{5.6}$$

See Figure B.2 for a visualization of Q on the larger slab that is analogous to Figure B.1.

5.3.2. Results

We begin with the smaller aspect ratio slab. Table A.1 lists the (non-dimensional) energies of the initial condition for each τ_0 compared to the energies of the equilibrium state (a local minimizer), for both homeotropic and planar degenerate anchoring.

Figure B.1 (middle column) depicts the final equilibrium solutions with homeotropic anchoring, all of which had very regular stripe patterns. In addition, as τ_0 increased, the final stripe patterns aligned more with the diagonal of the slab. This is most likely due to the zero Neumann condition imposed on the sides. If a periodic boundary condition were used, then the final configuration would be invariant to rotations of the $\mathbf{e}_1, \mathbf{e}_2$ plane. We were not able to enforce this condition because of a limitation of Firedrake.

For the planar degenerate anchoring case (Figure B.1, right column), similar striped patterns occurred in the equilibrium solutions for each twist value. However, the alignment with the diagonal was not quite as pronounced. Moreover, the transition between stripes was slightly different from the homeotropic case and the period was different. For instance, $\tau_0 = 20$ corresponds to an ideal period of $p = 2\pi/\tau_0 \approx 0.314$, but the measured period from the simulation was $p = 0.35$ ($p = 0.41$) for the homeotropic (planar degenerate) case. We also note that in the planar degenerate case, with $\tau_0 = 5$, we approximately see a circular region of tangential directors surrounding a center where the director becomes normal to $\mathbf{e}_3$. This is because the anchoring constants, which are set to $w_1 = w_2 = (1/\omega) = 10$, outweigh the twist.

Simulation times varied, ranging from 0 to 8 minutes for the homeotropic case, and

0 to 7 minutes for the planar degenerate case. There seemed to be no pattern with regard to which anchoring case led to longer simulation times.

For the larger slab, Table A.2 lists the (non-dimensional) energies of the initial condition for each τ_0 compared to the energies of the equilibrium state (a local minimizer), for both homeotropic and planar degenerate anchoring. Figure B.2 illustrates the final equilibrium solutions with homeotropic and planar degenerate anchoring, which shows very similar solutions as for the small slab. Again, the diagonal alignment was more pronounced for the homeotropic case. For example, for $\tau_0 = 20$, the homeotropic case yielded a period p of $p = 0.35$, while the planar degenerate case yielded $p = 0.38$. One major difference from the first set of simulations was that when $\tau_0 = 5$, the solution for the homeotropic case consisted of the director pointing normal to the surface on the entire domain. Simulation times varied, ranging from 0 to 41 hours for the homeotropic case, and 0 to 16 hours for the planar degenerate case. Times were generally shorter for the planar degenerate case.

5.4. Shell Configuration

5.4.1. Details

The domain Ω is a spherical annulus (shell), where two choices were used. For the first shell, we set $\Omega = \Omega_{\text{shell},0} := \mathcal{B}(\mathbf{0}, 1) \setminus \overline{\mathcal{B}}(\mathbf{0}, 0.9)$, where $\mathcal{B}(\mathbf{0}, r)$ is an open ball of radius r. For the finite element discretization Ω_h, we set the mesh size to be $h = 0.02$. For the initial condition, when $\tau_0 > 0$, we let $\mathbf{w} = \mathbf{w}(x_1, x_2, x_3)$ be given by

$$\mathbf{w} = (\cos(\tau_0 x_3), \sin(\tau_0 x_3), 0)^\dagger . \tag{5.7}$$

Then, similarly to the initial conditions for the slabs, we set $\mathbf{n} = \mathbf{w}/|\mathbf{w}|$ and

$$Q_0 = s_0 \left(\mathbf{n} \otimes \mathbf{n} - I/3\right). \tag{5.8}$$

For $\tau_0 = 0$, we let $\mathbf{n} = \mathbf{x}/|\mathbf{x}|$, and set Q_0 as in (5.8).

The far left column of Figures B.3 and B.4 depicts the initial condition, where the color corresponds to $|\mathbf{n} \cdot \mathbf{r}|$ with $\mathbf{r} = \mathbf{x}/|\mathbf{x}|$, i.e. the radial unit vector (see Section 5.2). The stripes in the initial condition form a spiral on the spherical boundary running top to bottom, with spacing inversely proportional to τ_0. Moreover, Figures B.3 and B.4 show the final equilibrium state of Q, corresponding to a local minimizer, for both homeotropic and planar degenerate anchoring for a range of twist values τ_0.

For the second shell, we set $\Omega = \Omega_{\text{shell},1} := \mathcal{B}(\mathbf{0}, 1) \setminus \overline{\mathcal{B}}(\mathbf{p}, 0.9)$, where $\mathbf{p} = (0, 0, 0.05)^\dagger$, i.e. an off-centered annulus. Our mesh size was again set to $h = 0.02$. We used the same initial condition here as in (5.8). Figures B.5 and B.6 show the initial condition, as well as the final equilibrium state, for a range of twist values.

We also performed another set of numerical experiments for the first shell, $\Omega = \Omega_{\text{shell},0}$, but with the initial condition set to Q_0 in (5.6). Figures B.7 and B.8 show the initial condition, as well as the final equilibrium state, for a range of twist values. We omitted the case of $\tau_0 = 0$, since the results were not appreciably different from the previous experiments.

5.4.2. Results

We begin with the centered shell $\Omega_{\text{shell},0}$ and initial condition (5.8). Table A.3 lists the (non-dimensional) energies of the initial condition for each τ_0 compared to the energies of the equilibrium state (a local minimizer), for both homeotropic and planar degenerate anchoring.

Figures B.3 and B.4 (middle column) depict the final equilibrium solutions with

homeotropic anchoring, where the spiral stripe pattern has a slight undulation. Moreover, the spirals meet as two "fingers" at the poles of the shell. The slice views show that the spiral pattern persists through the shell's thickness. For $\tau_0 = 5$, instead of a stripe pattern, the director $\mathbf{n}$ is radial pointing outward from the origin, because the anchoring strength outweighs the twist effect.

For the planar degenerate anchoring case (Figures B.3 and B.4 (right column)), similar striped patterns are present in the equilibrium solutions for each twist value. We note that the transition between stripes is slightly different from the homeotropic case (as for the slab). For $\tau_0 = 5$, the director field is mainly tangential, except for two "poles" where the director becomes normal to the surface of the shell. Again, this is because the anchoring constants outweigh the twist.

Each simulation time ranged from 0 to 26 hours for the homeotropic case, and 0 to 11 hours for the planar degenerate case (with an exception for $\tau_0 = 10$ which took nearly 20 hours). In general, higher twist correlates with longer simulation times, and the planar degenerate case took longer than the homeotropic case.

Next, we consider the off-centered shell $\Omega_{\text{shell},1}$ and initial condition (5.8). Table A.4 lists the (non-dimensional) energies of the initial condition for each τ_0 compared to the energies of the equilibrium state (a local minimizer), for both homeotropic and planar degenerate anchoring.

Figures B.5 and B.6 depict the final equilibrium solutions for both homeotropic and planar degenerate anchoring, which show similar stripe patterns as for the previous centered shell. But there are some differences. For $\tau_0 = 5$ with planar degenerate anchoring, the two "poles" where the director becomes normal to the surface are shifted down toward

the thicker part of the shell. For $\tau_0 = 10$ and homeotropic anchoring, the stripe pattern is absent at the top (thinnest) part of the shell; for planar degenerate, the spiral pattern is only present on the lower (thicker) half of the shell. For higher twists, the spiral patterns are similar to the previous (centered) shell. This is due to the interplay of the anchoring strength and the twist. Basically, there is not enough "room" in the thinnest part of the shell to develop a twist of the director field if τ_0 is not sufficiently large. Each simulation time ranged from 0 to 24 hours for the homeotropic case, and 2 to 80 hours for the planar degenerate case. In general, higher twist correlates with longer simulation times, and the planar degenerate case took longer than the homeotropic case. For example, with $\tau_0 = 0$, it took around 30 minutes for the homeotropic case, and 32 hours for the planar degenerate case.

We now reconsider the centered shell $\Omega_{\text{shell},0}$ but with the initial condition (5.6). Table A.5 lists the (non-dimensional) energies of the initial condition for each τ_0 compared to the energies of the equilibrium state (a local minimizer), for both homeotropic and planar degenerate anchoring.

Figures B.7 and B.8 depict the final equilibrium solutions for both homeotropic and planar degenerate anchoring, which show similar stripe patterns as before. However, the stripe patterns break away from being a spiral in some cases. For instance, with homeotropic anchoring and $\tau_0 = 15, 20$, we see multiple triple junctions of the blue region. In addition, we see similar triple junctions for the planar degenerate anchoring with $\tau_0 = 15$. The $\tau_0 = 10$ case (planar degenerate) exhibits a somewhat bizarre hexagonal pattern with a slightly lower energy than the minimizer in Figures B.3 and B.4 ($\mathcal{E} = -66.795$ vs. $\mathcal{E} = -62.482$). Despite redoing this case with a finer mesh size of $h = 0.015$, the

pattern persisted (with a final energy of $\mathcal{E} = -68.244$), suggesting that this may represent a true minimizer. The other cases exhibited a similar spiral pattern as before. Each simulation took from 1 to 33 hours for the homeotropic case, and 4 to 14 hours for the planar degenerate case, with the latter case generally taking a shorter time than the former.

5.5. Comments on computing minimizers

We demonstrate the ramifications of Theorem 13, which has a mesh size restriction, on the form of discrete minimizers. Because of the non-convex terms in the energy, i.e. the double well and cholesteric term, the choice of mesh size affects more than just the resolution of the features of the minimizer Q. Indeed, too coarse a mesh can yield discrete minimizers that contain numerical artifacts, i.e. the "minimizer" may be very far from a true minimizer of the continuous problem. Figure B.9 show two simulations, one for the slab and one for shell, that illustrate how these numerical artifacts may manifest. In other words, when the mesh size is too large, the energy landscape of the discrete energy functional may contain artificial minima, so the gradient flow finds a different minimizer with a very different structure.

We also consider another type of perturbation of the initial condition in Figure B.10. Here, a centered shell, with homeotropic anchoring, is considered with $\tau_0 = 15$, but the initial condition corresponds to $\tau_0 = 25$, i.e. more tightly packed stripes. Because of this mismatch of the initial condition, the simulation took approximately 1 week to "unwind" the extra twist in the initial condition to arrive at a minimizer with $\tau_0 = 15$. Moreover, the gradient flow obtained a different minimizer ($\mathcal{E} = -151.78$) with a stripe pattern that contained two triple junctions, as opposed to Figure B.3 ($\mathcal{E} = -151.98$) which

had no triple junctions.

5.6. Other Cholesteric Model

We attempted to reproduce a result produced by Lavrentovich and Tran in [60, Fig. 6], which models a cholesteric shell with outer radius 0.42 μm and inner radius 0.24 μm. From this, we choose the characteristic length $\xi = 0.42$ μm.

The dimensional parameters used are for the 5CB liquid crystal, which can be found in [78]. The double well constants are $a_2 = 0.172 \times 10^6$ J/m^3, $a_3 = 2.12 \times 10^6$ J/m^3, and $a_4 = 1.73 \times 10^6$ J/m^3. Following Section 2.3, we then calculate $c_0 = 0.038362224 \times 10^6$ J/m^3, and divide the double well coefficients by c_0 to obtain the non-dimensional double well:

$$a_0 = 1.0, \quad a_2 = 4.4835774, \quad a_3 = 55.262698, \quad a_4 = 45.096447,$$

which gives $s_0 = 0.7992969$.

For the elastic coefficients (for 5CB in [78]), we have $\breve{\ell}_1 = \breve{\ell}_2 = 4 \times 10^{-11}$ J/m, $\breve{\ell}_{24} = 0$. Since $\breve{\ell}_{24} = 0$, this corresponds, via the mapping of the constants in Section 2.4, to $\ell_1 = \ell_2 = 4 \times 10^{-11}$ J/m, $\ell_3 = -4 \times 10^{-11}$ J/m. From here, we choose $\ell_m = 4 \times 10^{-11}$ J/m and divide by ℓ_m to obtain $\ell_1 = \ell_2 = 1$, $\ell_3 = -1$. Note that the inequalities in (3.3) are not strictly satisfied in this case. We also have a cholesteric pitch of $p = 0.18$ μm, and so the non-dimensional twist is $\tau_0 = 14.660766$. The anchoring condition is planar degenerate with $w_0 = 0$, $w_1 = 4 \times 10^{-4}$ J/m^2, $w_2 = 8 \times 10^{-4}$ J/m^2. Multiplying the first two by ξ/ℓ_m, we obtain $w_0 = 0$, $w_1 = 4.2$. Finally, using the formulas $\eta = \sqrt{\ell_m/(c_0\xi^2)}$ and $\omega = \ell_m/(w_2\xi)$, we have that $\eta = 0.07688273$ and $\omega = 0.11904762$.

We ran simulations for the above parameters using the following three models: A,

B-1, B-2. Model A is given in (2.7) (see [68, 70, 78]), and model B-1 is the cholesteric model in [88] and discussed in Section 2.4. Since s_0 is inconsistent with their *effective* double well $\widetilde{\psi}$ (see Section 2.4.2 and the discussion about the extra $\mathrm{tr}(Q^2)$ term), we ran the simulation for a model B-2, which is identical to B-1, except that we replace s_0 with the correct global minimum $\widetilde{s_0}$ for $\widetilde{\psi}$.

The energy results of these simulations are found in Table A.6, and the results of the simulation using model A are found in Figure B.11, which does not exactly match the result in [60, Fig. 6]. Their method uses a conjugate gradient method which is different from our minimization scheme, i.e. their method travels along a different path in the energy landscape so finds a different local minimizer.

We do not give the visualization of the other two models (B-1, B-2), because they look *nearly identical* to Model A. We suspect this is due to the cholesteric twist having a dominant effect. It should be noted, however, that models A and B-1, B-2 differ greatly in their final energies, as well as in the values of the maximum eigenvalue $\bar{\lambda}$ of Q, the latter of which is shown in Figure B.12. We emphasize that, due to the energetic differences, if other physics were to be coupled to the liquid crystal (e.g. electro-static effects), then the models would most likely give vastly different equilibrium states. In addition, if the twist parameter is sufficiently large, then the effective bulk potential (recall Section 2.4 (2.4.2)) will favor an isotropic state, which is not consistent with cholesteric LC behavior [88, 60, 81].

It took approximately 2 hours to simulate model A, while it took about 40 minutes to simulate models B-1 and B-2. The mesh size used was 0.04285714.

Chapter 6. Conclusions

The first part of this thesis gives an overview of the Landau-de Gennes (LdG) model [68, 70, 78] for nematic LCs, with cholesteric effects, and connects it to a slightly different cholesteric model in [88]. We then presented a gradient flow and numerical scheme for the cholesteric LdG model. An adaptive time-stepping strategy was used to reduce the computation time. We also derived time-step restrictions to have an energy decreasing algorithm, restrictions which indicate that the classic convex splitting approach is not uniformly stable in the presence of the cholesteric twist. Moreover, we showed that a mesh size restriction is necessary to ensure that discrete minimizers are approximate versions of isolated, true minimizers.

Using our gradient flow, we computed (local) minimizers with an adaptive time-stepping strategy to reduce the computation time. This produced several numerical simulations that illustrate the rich behavior of the cholesteric LdG model. For both slab and shell geometries, the minimizer has regular stripe patterns that are affected by the domain shape. Specifically, the off-centered shell has a very different minimizer than the centered shell for intermediate values of the twist τ_0. We also demonstrate that our gradient flow scheme can compute different (local) minimizers for the same set of parameters but depending on the initial condition. Some of the simulations show perturbed stripe patterns that exhibit "triple junctions" of the stripe and are due to using initial conditions with a high spatial frequency. All of these (equilibrium) stripe patterns are in line with known experiments for cholesteric LCs (for instance, see [34, 36] for examples with thin slab geometries, and [88, 60, 59, 81] for shell geometries).

We also gave examples of how artificial solutions may arise if the mesh size is not

small enough, i.e. the computed minimizer may exhibit discrete artifacts. Furthermore, we showed that the two cholesteric models exhibit very different energies, though the computed solution may still have a very similar configuration of the director $\mathbf{n}$.

The results of this thesis should help inform LC computational scientists about potential pitfalls in the simulation of the cholesteric LdG model and lead to more robust numerical predictions of cholesteric LC physics.

Appendix A. Tables

	Homeotropic anchoring		**Planar degenerate anchoring**	
τ_0	*Initial energy*	*Final energy*	*Initial energy*	*Final energy*
0	9.80015487	8.21500396	0.0	0.0
5	2.19357782	-0.91492417	0.73088994	-3.10989917
10	-4.33873728	-10.98108043	-6.50203019	-14.33213509
15	-15.42302005	-31.95613716	-16.98598006	-34.85051092
20	-28.16438688	-65.69156577	-30.05907645	-68.243013

Table A.1. Energies for the small slab ($1 \times 1 \times 0.2$) in Figure B.1 (Sec. 5.3.2).

	Homeotropic anchoring		**Planar degenerate anchoring**	
τ_0	*Initial energy*	*Final energy*	*Initial energy*	*Final energy*
0	39.20061947	32.86058337	0.0	0.0
5	49.25887441	-2.64966269	43.13556899	-11.06811563
10	70.41495358	-41.83731193	65.18722048	-51.78216459
15	104.88188461	-122.7420167	100.38078589	-133.893747
20	151.32789951	-254.83515683	147.15907691	-265.87890179

Table A.2. Energies for the large slab ($2 \times 2 \times 0.2$) in Figure B.2 (Sec. 5.3.2).

	Homeotropic anchoring		**Planar degenerate anchoring**	
τ_0	*Initial energy*	*Final energy*	*Initial energy*	*Final energy*
0	1.23566209	1.23349847	56.94106826	51.13769725
5	60.49129983	1.23349741	12.23300007	-13.13068291
10	21.34536007	-33.76001607	-26.81216759	-62.48198396
15	-36.59992963	-151.97707415	-84.58904161	-185.01096392
20	-103.25794942	-348.22427414	-151.0115368	-384.49961726
25	-166.11557298	-639.23581796	-213.57414074	-677.04411588

Table A.3. Energies for the centered shell ($\Omega_{\text{shell},0}$) in Figures B.3 and B.4 (Sec. 5.4.2).

	Homeotropic anchoring		**Planar degenerate anchoring**	
τ_0	*Initial energy*	*Final energy*	*Initial energy*	*Final energy*
0	1.34958562	1.26765658	56.95232872	1.56772626
05	60.4884546	1.24104888	12.23023189	-13.2233694
10	21.30137144	-34.07603296	-26.85588133	-64.03286781
15	-36.81485612	-149.89711829	-84.80477055	-182.77158029
20	-103.91110362	-342.9675383	-151.66656546	-379.13022842
25	-167.63544101	-630.70950725	-215.09203743	-668.63027357

Table A.4. Energies for the off-centered shell ($\Omega_{\text{shell},1}$) in Figures B.5 and B.6 (Sec. 5.4.2).

	Homeotropic anchoring		**Planar degenerate anchoring**	
τ_0	*Initial energy*	*Final energy*	*Initial energy*	*Final energy*
5	107.21684588	1.23349885	65.88019321	-12.85142139
10	143.69128926	-33.21147874	103.37532314	-66.79504813
15	198.33754579	-151.71328798	158.2365114	-185.18312273
20	269.46171783	-348.4203652	229.41729719	-384.3815465
25	352.2492802	-639.0239269	312.42189391	-676.81099557

Table A.5. Energies for the centered shell ($\Omega_{\text{shell},0}$), with oscillatory initial condition, in Figures B.7 and B.8 (Sec. 5.4.2).

Model	*Initial energy*	*Final energy*
A	-196.83349123	-479.36144656
B-1	310.00570697	185.52404418
B-2	365.134880212	183.86282819

Table A.6. Energies for the model comparisons in Figures B.11 and B.12 (Sec. 5.6).

Appendix B. Simulation Figures

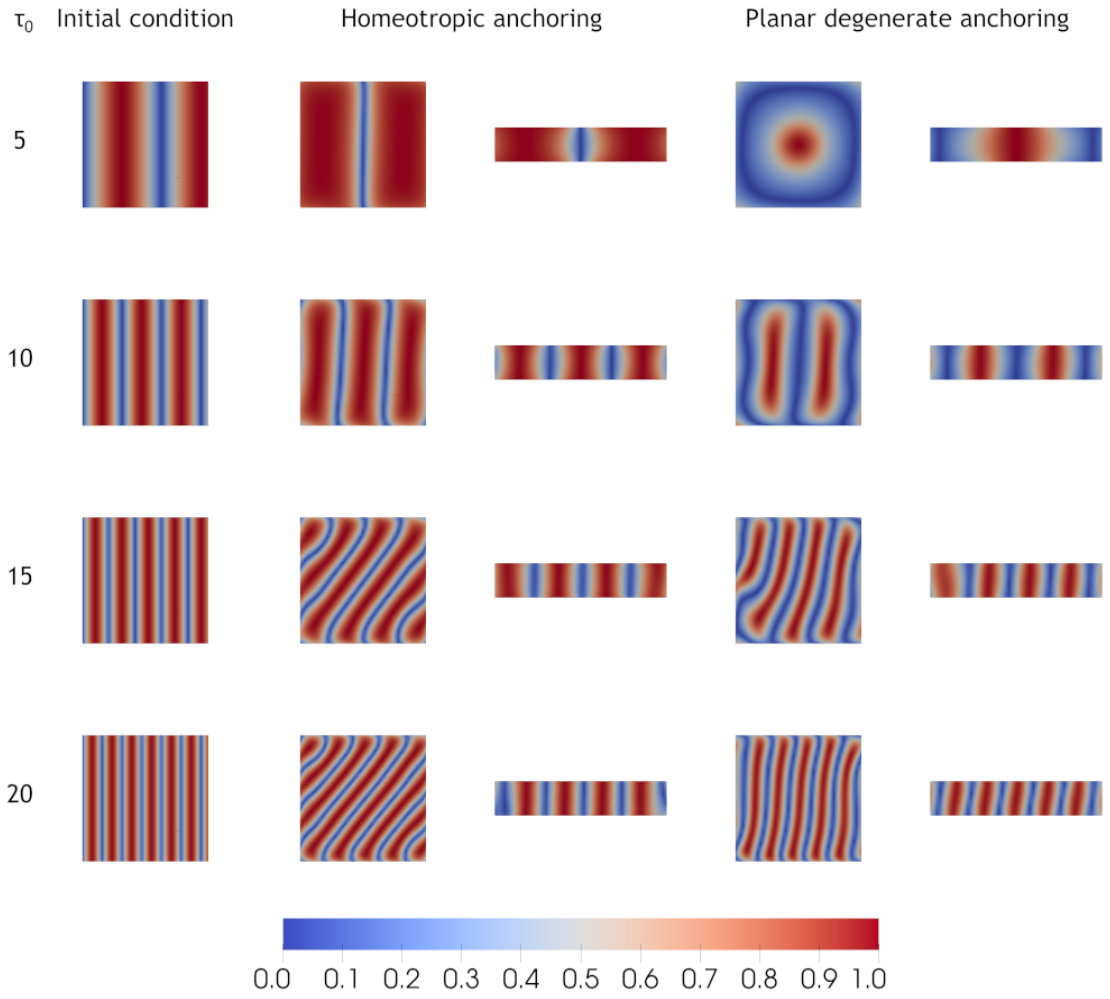

Figure B.1. Small aspect ratio slab: $1 \times 1 \times 0.2$ (Sec. 5.3.2). Color is proportional to $|\mathbf{n} \cdot \mathbf{e}_3|$. Initial condition column shows top view (viewing the xy plane) of slab. Homeotropic anchoring columns show the top view and a vertical slice (viewing the xz plane) through the middle of the slab. Planar degenerate anchoring columns have the same format.

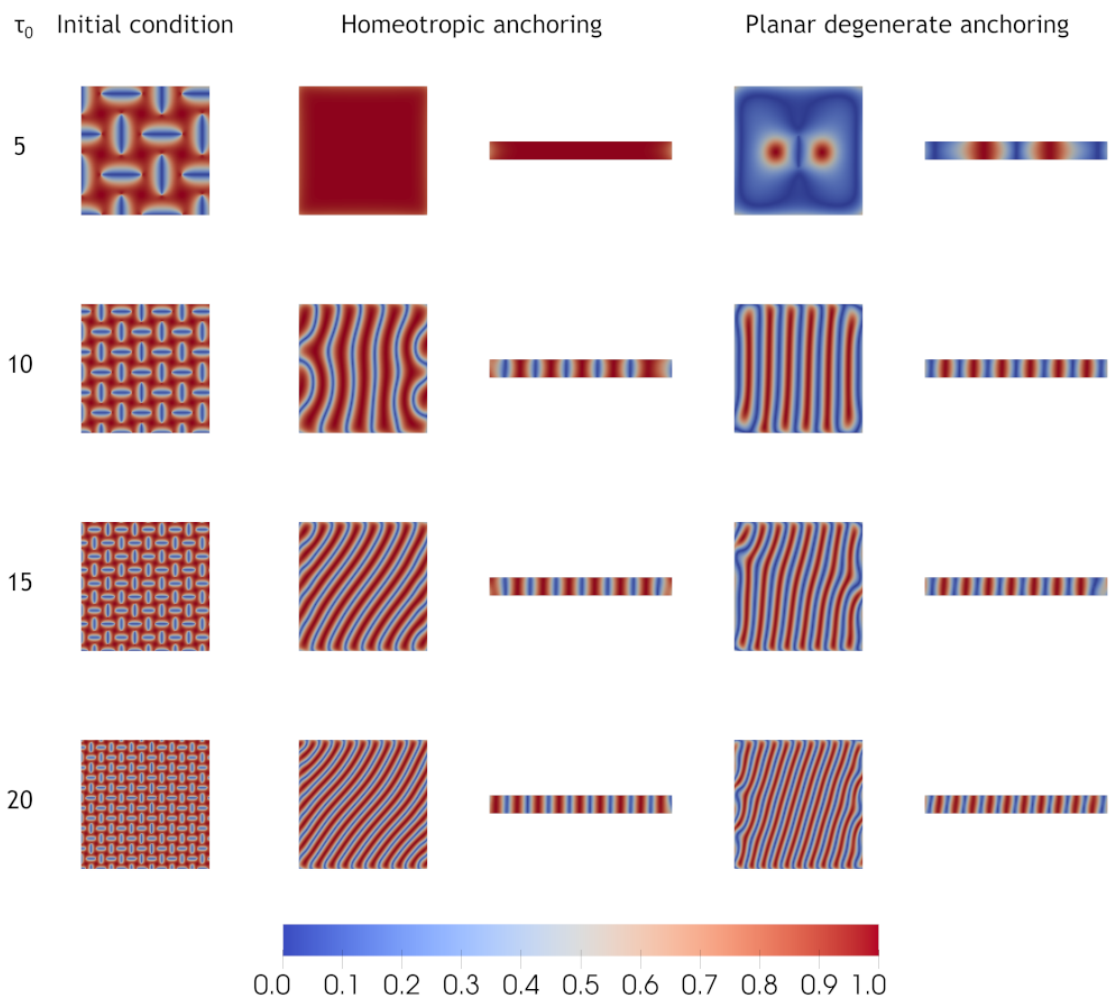

Figure B.2. Large aspect ratio slab: $2 \times 2 \times 0.2$ (Sec. 5.3.2). Color is proportional to $|\mathbf{n} \cdot \mathbf{e}_3|$. Similar format to Figure B.1.

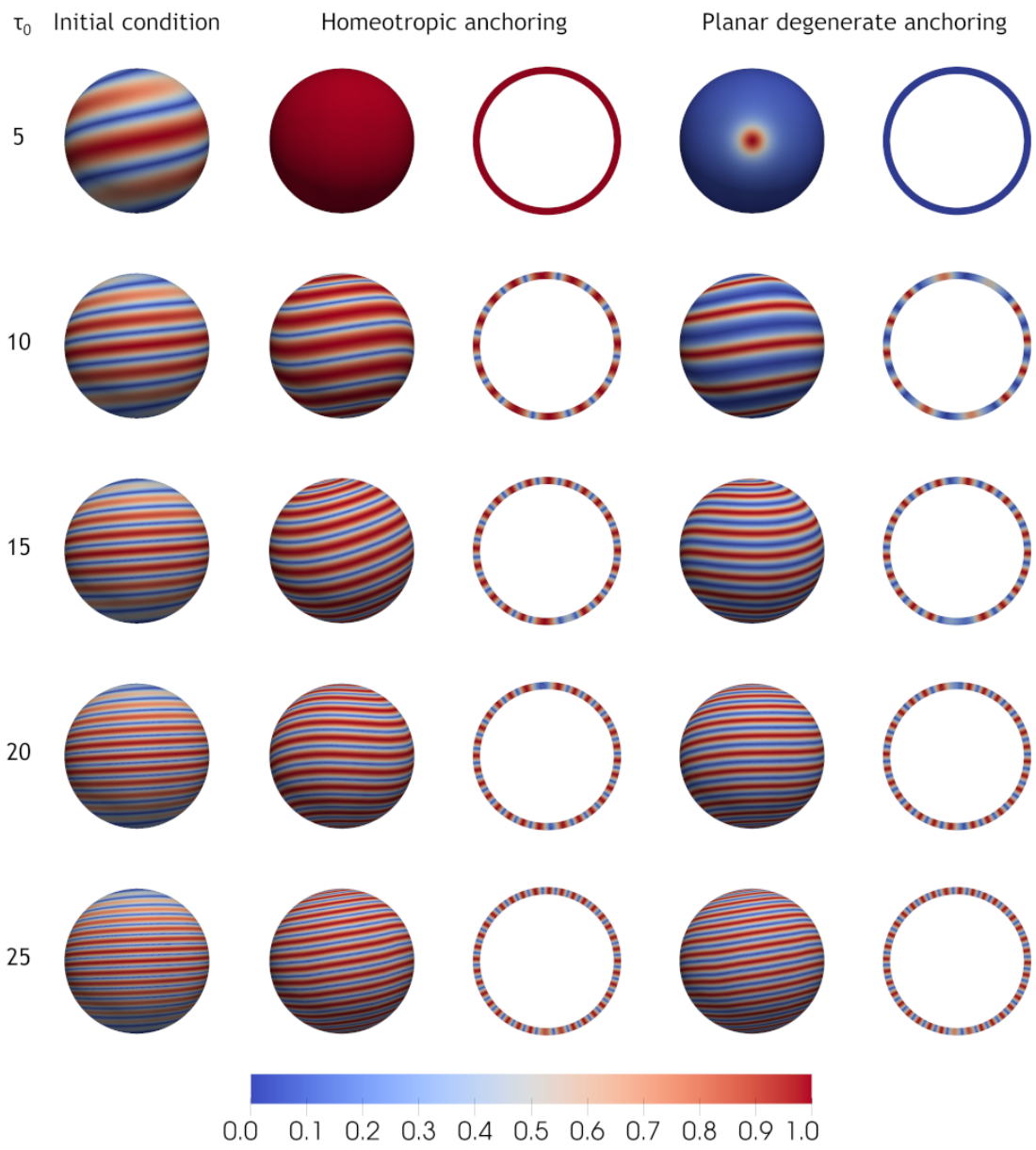

Figure B.3. Centered shell ($\Omega_{\text{shell},0}$), front view (viewing the yz plane) (Sec. 5.4.2). Color is proportional to $|\mathbf{n} \cdot \mathbf{r}|$ with $\mathbf{r} = \mathbf{x}/|\mathbf{x}|$. Homeotropic anchoring columns show the outer boundary and a vertical slice through the shell. Planar degenerate anchoring columns have the same format.

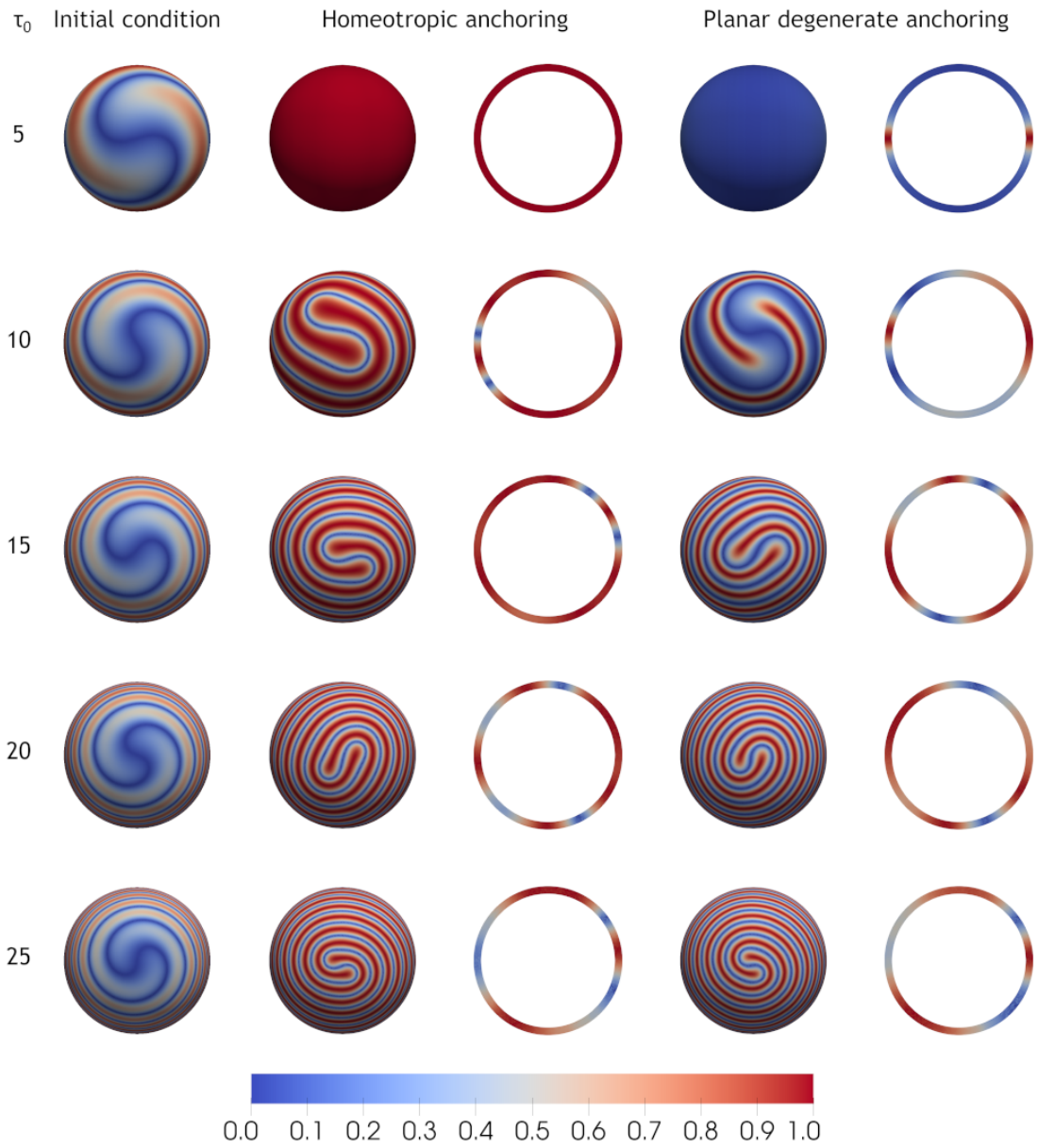

Figure B.4. Centered shell ($\Omega_{\text{shell},0}$), top view (viewing the xy plane) (Sec. 5.4.2). Similar format to Figure B.3; the slices are parallel to the view plane.

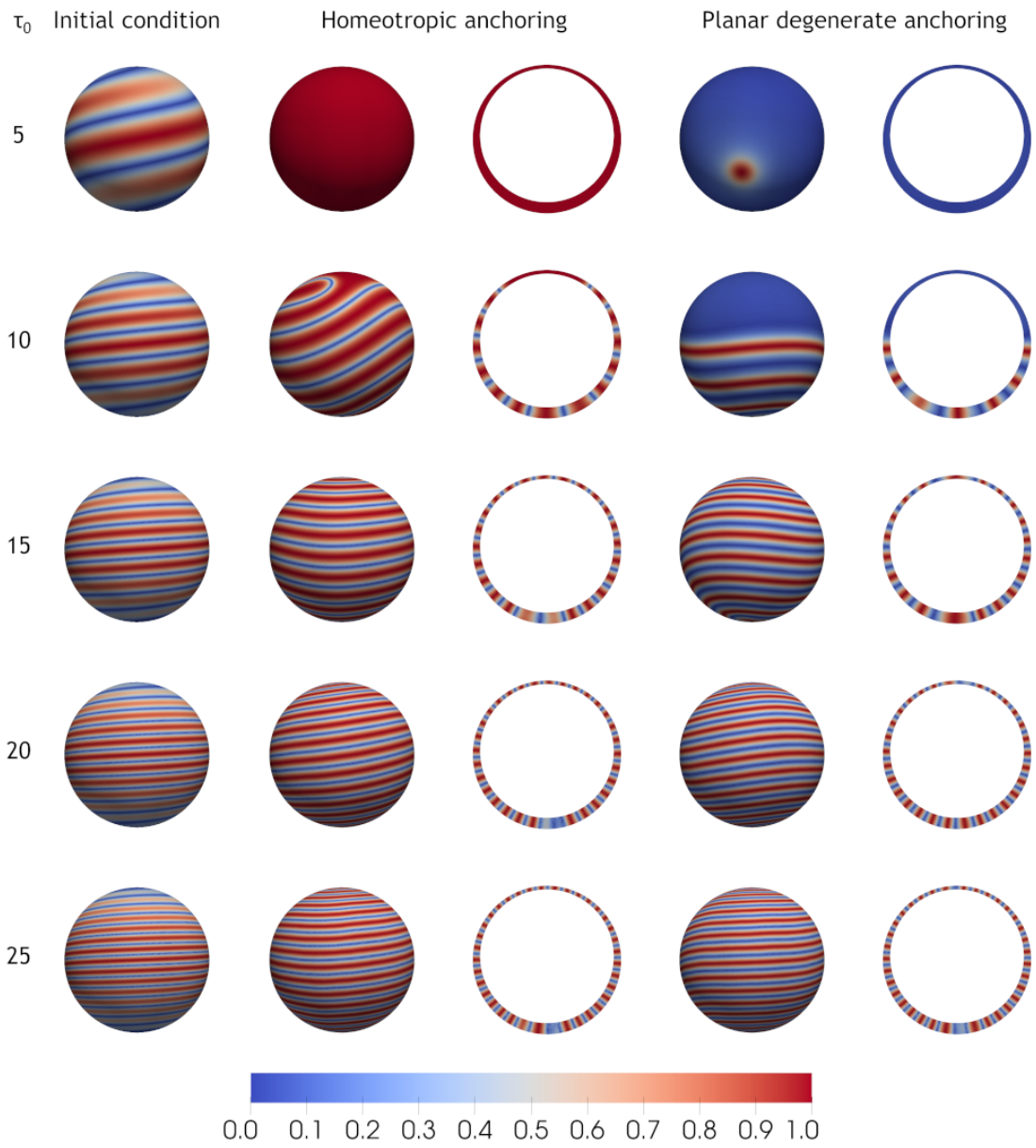

Figure B.5. Off-centered shell ($\Omega_{\text{shell},1}$), front view (Sec. 5.4.2). Similar format to Figure B.3.

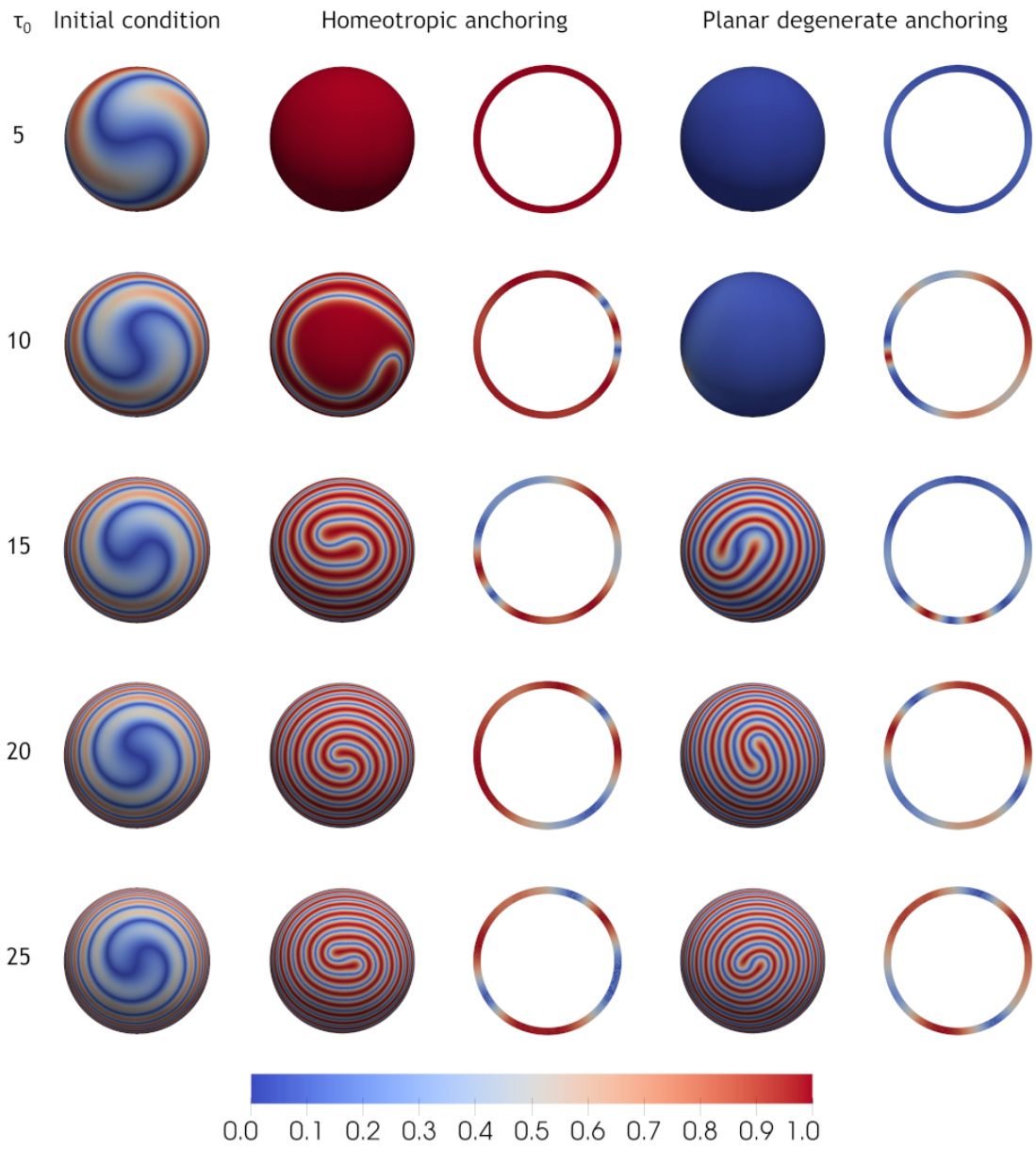

Figure B.6. Off-centered shell ($\Omega_{\text{shell},1}$), top view (Sec. 5.4.2). Similar format to Figure B.4.

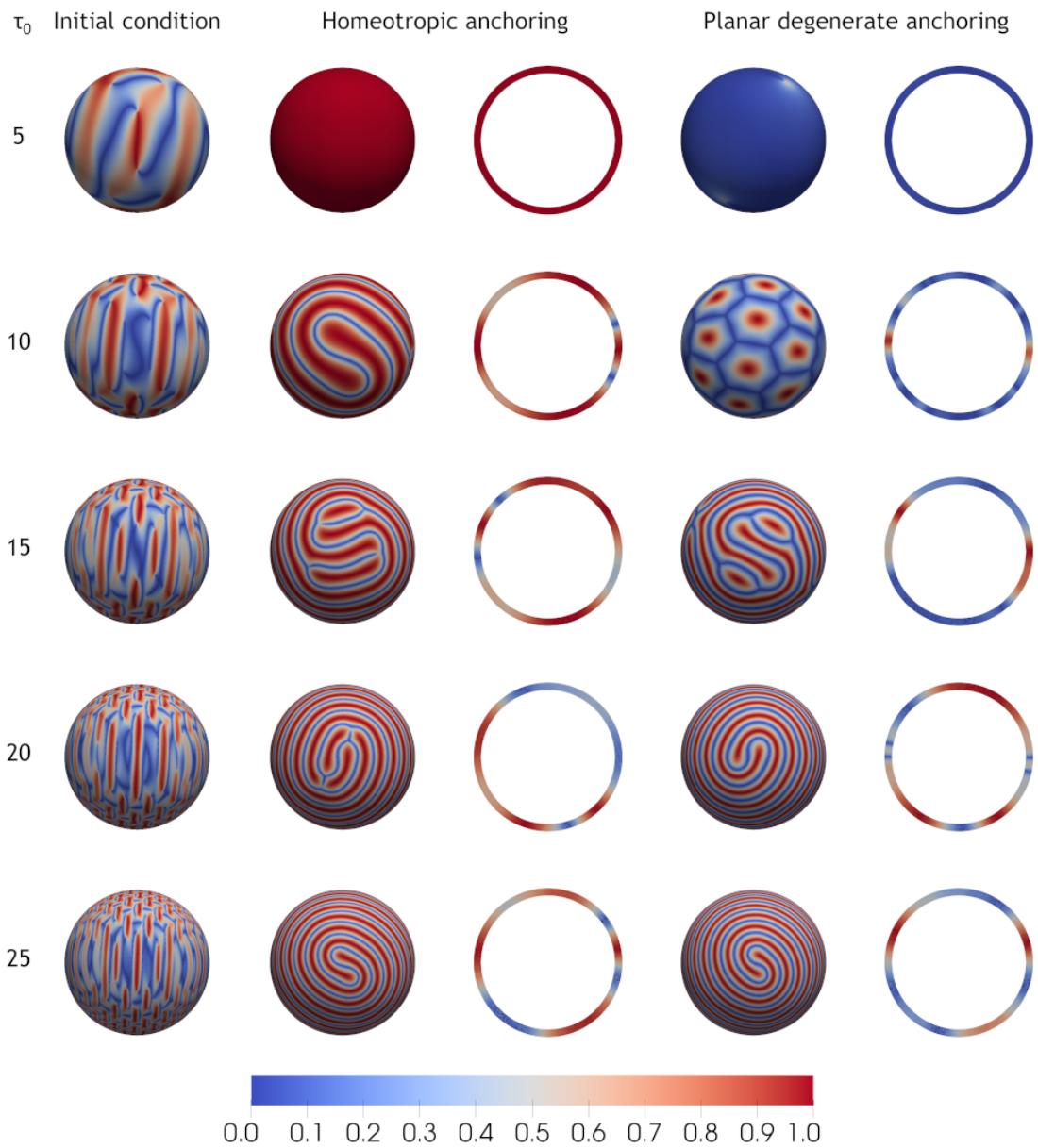

Figure B.7. Centered shell ($\Omega_{\text{shell},0}$) with oscillatory initial condition, front view (viewing the yz plane) (Sec. 5.4.2). Similar format to Figure B.3.

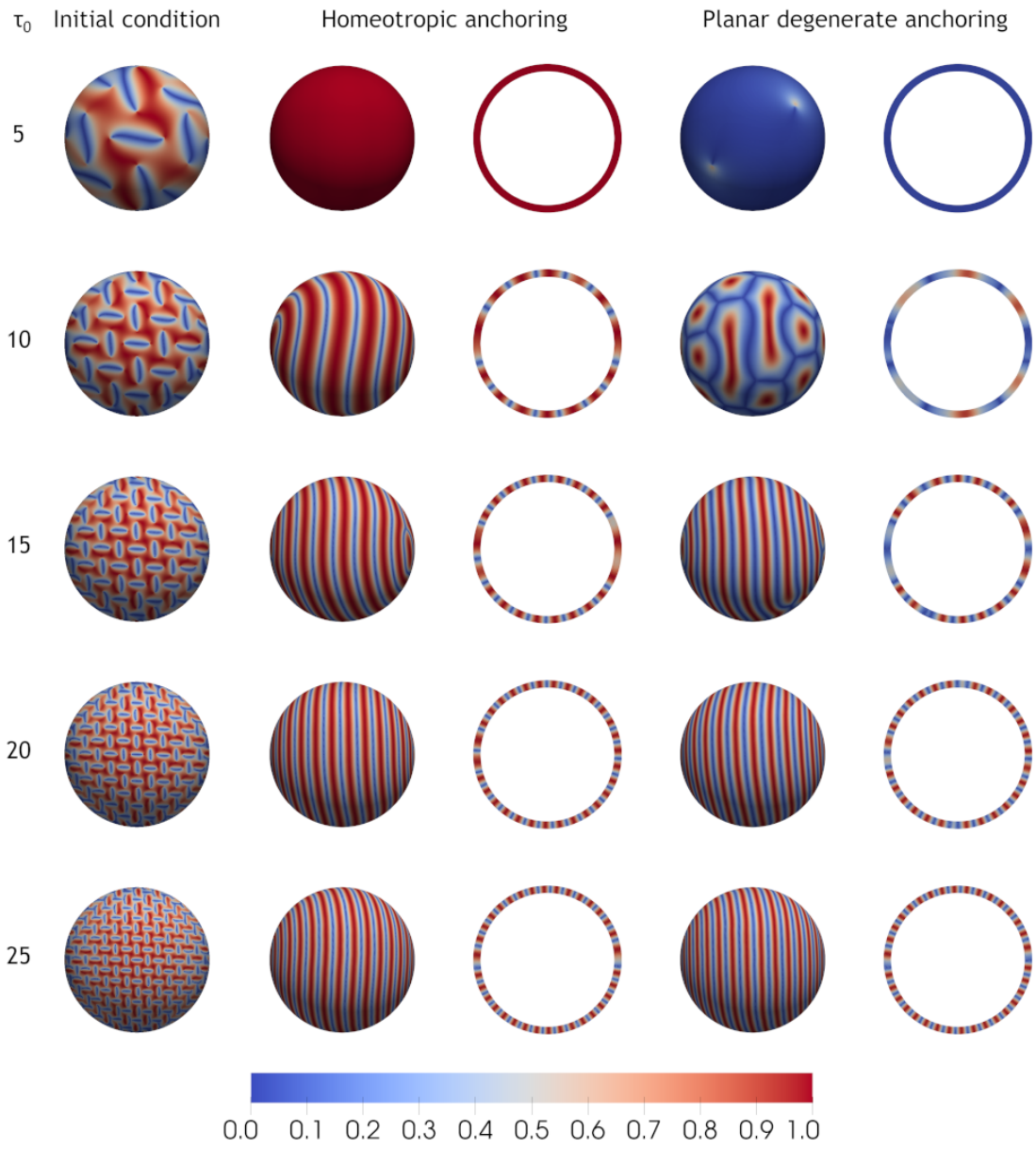

Figure B.8. Centered shell ($\Omega_{\text{shell},0}$) with oscillatory initial condition, top view (viewing the xy plane) (Sec. 5.4.2). Similar format to Figure B.4. The choice of the initial condition caused the local minimizer to have a different orientation relative to the previous plots.

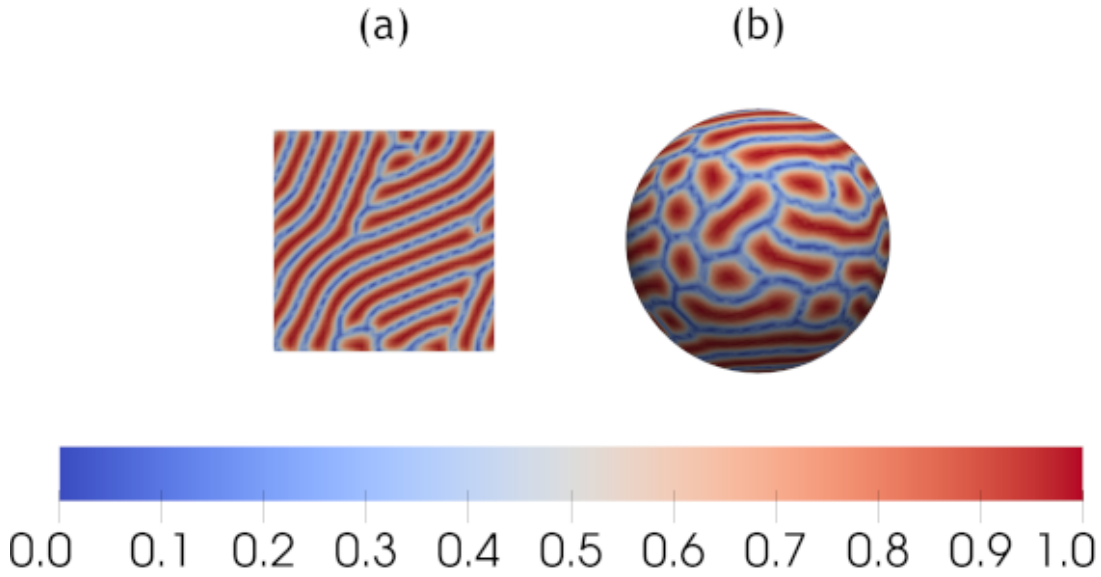

Figure B.9. Equilibrium states when the mesh size is not small enough (Sec. 5.5). Example (a) shows an energy minimizer, with $\mathcal{E} = -213.62$, for the large slab with the oscillatory initial condition and $\tau_0 = 20$, but with a mesh size of 0.05 (cf. Figure B.2 (homeotropic), with $\mathcal{E} = -254.84$, that used a mesh size of 0.02). Clearly, the period of the stripes in Figure B.2 is much smaller than in (a) (to be exact, the period here is around 0.576). Example (b) shows a minimizer, with $\mathcal{E} = -757.69$, for the centered shell with the periodic initial condition and $\tau_0 = 25$, but with a mesh size of 0.05 and a shell thickness of 0.2 (cf. Figure B.3 (homeotropic), with $\mathcal{E} = -639.24$, that used a mesh size of 0.02 and a thickness of 0.1). Even though all other parameters were the same, the gradient flow finds a different minimizer with a very different structure.

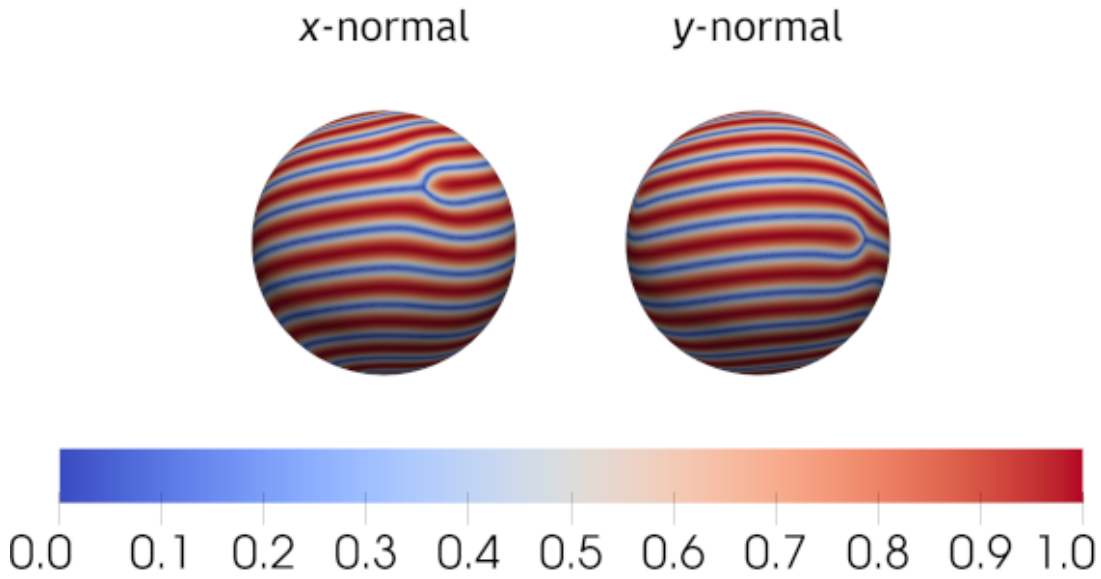

Figure B.10. Different equilibrium states with mismatched initial condition (Sec. 5.5). We consider a centered shell with homeotropic anchoring and a twist of $\tau_0 = 15$ (recall Figure B.3 (homeotropic)). However, we use a periodic initial condition consistent with $\tau_0 = 25$ (see far left col. in Figure B.3), i.e. more stripes than the minimizer should have. The computed minimizer has energy $\mathcal{E} = -151.78$, compared to $\mathcal{E} = -151.98$ in Figure B.3 (homeotropic), and contains two triple junctions not present in the previous simulation.

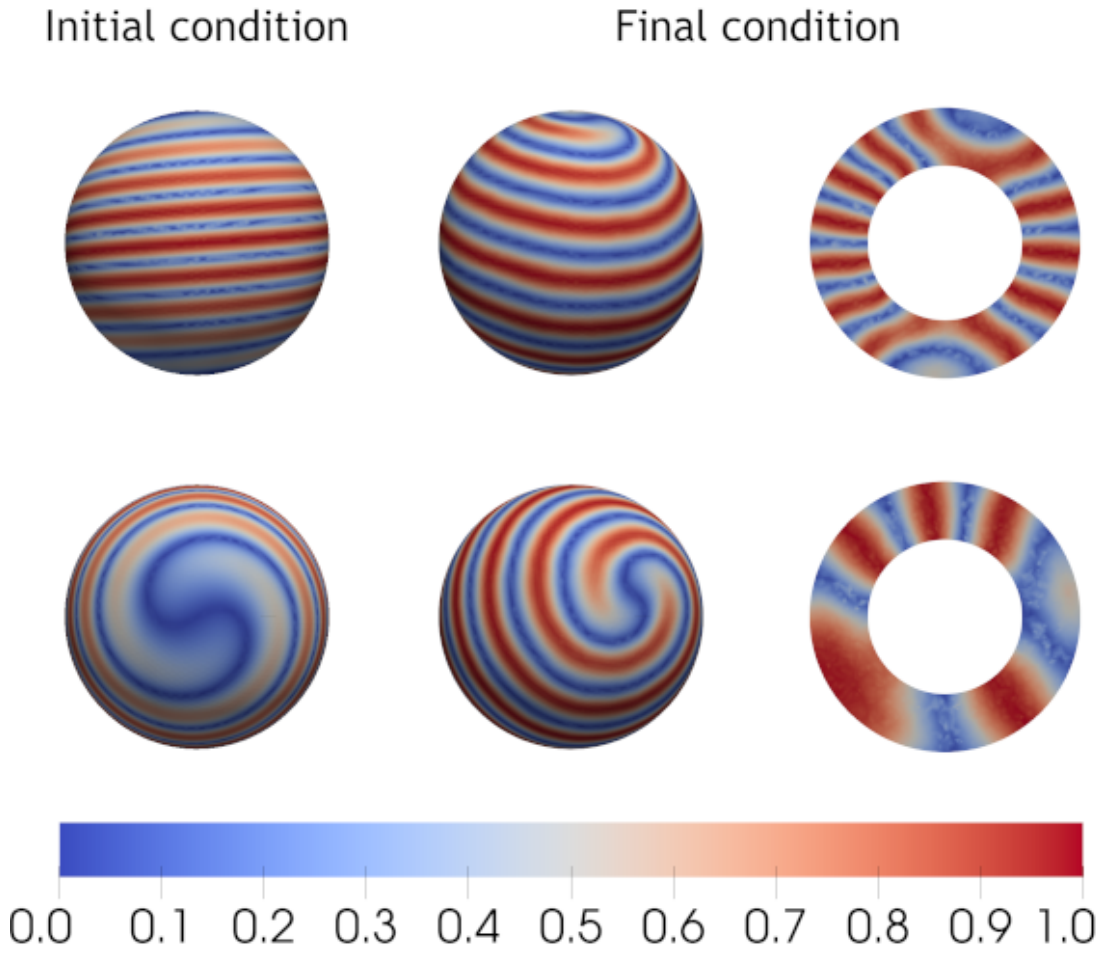

Figure B.11. Results from the simulation of Model A (Sec. 5.6). Both a front view (viewing the yz plane) and a top view (viewing the xy plane) are shown, with a view of the initial condition and final state (both outside view and slice are shown). Models B-1 and B-2 had visually indistinguishable patterns.

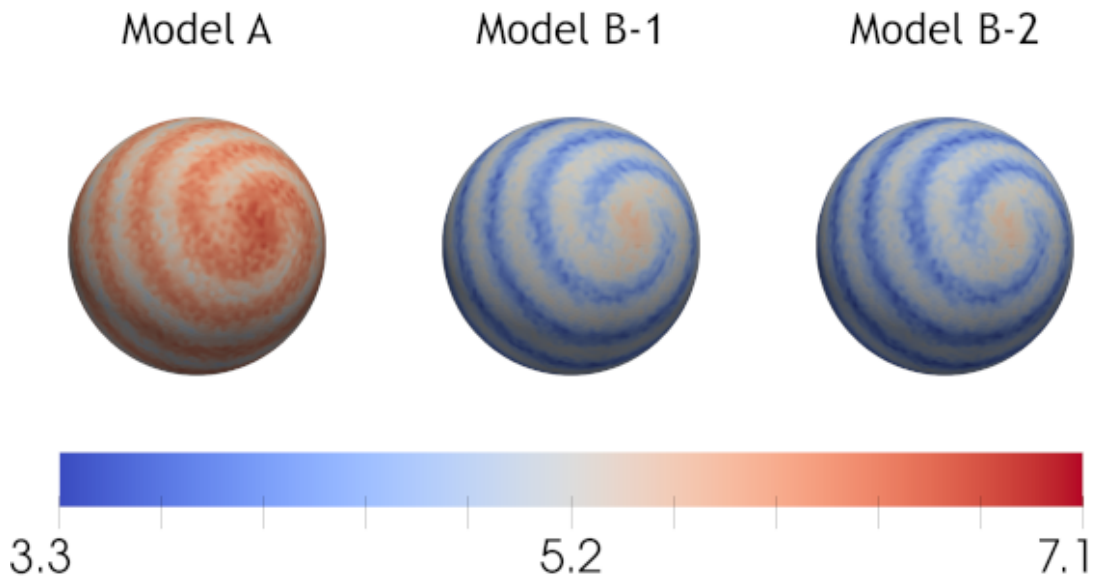

Figure B.12. Results from the simulation of Models A, B-1, B-2 (Sec. 5.6), except viewing the largest eigenvalue $\bar{\lambda} = \max\{\lambda_i\}_{i=1}^{3}$ of the energy minimizing Q. We have Model A (our formulation), Model B-1, (their formulation with their inconsistent s_0), and Model B-2 (their formulation with a consisent s_0).

Bibliography

[1] J. H. Adler, T. J. Atherton, T. R. Benson, D. B. Emerson, and S. P. MacLachlan. Energy minimization for liquid crystal equilibrium with electric and flexoelectric effects. *SIAM Journal on Scientific Computing*, 37(5):S157–S176, 2015.

[2] J. H. Adler, T. J. Atherton, D. B. Emerson, and S. P. MacLachlan. An energy-minimization finite-element approach for the frank–oseen model of nematic liquid crystals. *SIAM Journal on Numerical Analysis*, 53(5):2226–2254, 2015.

[3] J. H. Adler, D. B. Emerson, S. P. MacLachlan, and T. A. Manteuffel. Constrained optimization for liquid crystal equilibria. *SIAM Journal on Scientific Computing*, 38(1):B50–B76, 2016.

[4] Gonzague Agez, Chloé Bayon, and Michel Mitov. Multiwavelength micromirrors in the cuticle of scarab beetle chrysina gloriosa. *Acta Biomaterialia*, 48:357–367, 2017.

[5] Ágnes Buka and Nándor Éber, editors. *Flexoelectricity in Liquid Crystals: Theory, Experiments and Applications*. World Scientific, 2012.

[6] James Ahrens, Berk Geveci, and Charles Law. ParaView: An end-user tool for large data visualization. In *Visualization Handbook*. Elesvier, 2005. ISBN 978-0123875822.

[7] Francois Alouges. A new algorithm for computing liquid crystal stable configurations: The harmonic mapping case. *SIAM Journal on Numerical Analysis*, 34(5):pp. 1708–1726, 1997.

[8] Iztok Bajc, Frédéric Hecht, and Slobodan Žumer. A mesh adaptivity scheme on the Landau–de Gennes functional minimization case in 3D, and its driving efficiency. *Journal of Computational Physics*, 321:981 – 996, 2016.

[9] Satish Balay, Shrirang Abhyankar, Mark F. Adams, Steven Benson, Jed Brown, Peter Brune, Kris Buschelman, Emil Constantinescu, Lisandro Dalcin, Alp Dener, Victor Eijkhout, Jacob Faibussowitsch, William D. Gropp, V'aclav Hapla, Tobin Isaac, Pierre Jolivet, Dmitry Karpeev, Dinesh Kaushik, Matthew G. Knepley, Fande Kong, Scott Kruger, Dave A. May, Lois Curfman McInnes, Richard Tran Mills, Lawrence Mitchell, Todd Munson, Jose E. Roman, Karl Rupp, Patrick Sanan, Jason Sarich, Barry F. Smith, Stefano Zampini, Hong Zhang, Hong Zhang, and Junchao Zhang. PETSc/TAO users manual. Technical Report ANL-21/39 - Revision 3.19, Argonne National Laboratory, 2023.

[10] Satish Balay, Shrirang Abhyankar, Mark F. Adams, Jed Brown, Peter Brune, Kris Buschelman, Lisandro Dalcin, Victor Eijkhout, William D. Gropp, Dinesh Kaushik, Matthew G. Knepley, Lois Curfman McInnes, Karl Rupp, Barry F. Smith, Stefano Zampini, Hong Zhang, and Hong Zhang. PETSc Web page. `http://www.mcs.anl.`

gov/petsc, 2016.

[11] Satish Balay, William D. Gropp, Lois Curfman McInnes, and Barry F. Smith. Efficient management of parallelism in object oriented numerical software libraries. In E. Arge, A. M. Bruaset, and H. P. Langtangen, editors, *Modern Software Tools in Scientific Computing*, pages 163–202. Birkhäuser Press, 1997.

[12] G. Barbero and G. Durand. On the validity of the rapini-papoular surface anchoring energy form in nematic liquid crystals. *J. Phys. France*, 47(12):2129–2134, 1986.

[13] John W. Barrett, Xiaobing Feng, and Andreas Prohl. Convergence of a fully discrete finite element method for a degenerate parabolic system modelling nematic liquid crystals with variable degree of orientation. *ESAIM: Mathematical Modelling and Numerical Analysis*, 40:175–199, 1 2006.

[14] Sören Bartels and Alexander Raisch. Simulation of Q-tensor fields with constant orientational order parameter in the theory of uniaxial nematic liquid crystals. In Michael Griebel, editor, *Singular Phenomena and Scaling in Mathematical Models*, pages 383–412. Springer International Publishing, 2014.

[15] J.S. Biggins, M. Warner, and K. Bhattacharya. Elasticity of polydomain liquid crystal elastomers. *Journal of the Mechanics and Physics of Solids*, 60(4):573 – 590, 2012.

[16] Paolo Biscari and Pierluigi Cesana. Ordering effects in electric splay freedericksz transitions. *Continuum Mechanics and Thermodynamics*, 19(5):285–298, 2007.

[17] L.M. Blinov. *Electro-optical and magneto-optical properties of liquid crystals*. Wiley, 1983.

[18] Juan-Pablo Borthagaray, Ricardo H. Nochetto, and Shawn W. Walker. A structure-preserving FEM for the uniaxially constrained **Q**-tensor model of nematic liquid crystals. *Numerische Mathematik*, 145:837 – 881, 2020.

[19] Juan Pablo Borthagaray and Shawn W. Walker. Chapter 5 - the Q-tensor model with uniaxial constraint. In Andrea Bonito and Ricardo H. Nochetto, editors, *Geometric Partial Differential Equations - Part II*, volume 22 of *Handbook of Numerical Analysis*, pages 313 – 382. Elsevier, 2021.

[20] Andrea Braides. *Gamma-Convergence for Beginners*, volume 22 of *Oxford Lecture Series in Mathematics and Its Applications*. Oxford Scholarship, 2002.

[21] Susanne C. Brenner and L. Ridgway Scott. *The Mathematical Theory of Finite Element Methods*, volume 15 of *Texts in Applied Mathematics*. Springer, New York, NY, 3rd edition, 2008.

[22] Haïm Brezis, Jean-Michel Coron, and Elliott H. Lieb. Harmonic maps with defects. *Communications in Mathematical Physics*, 107(4):649–705, 1986.

[23] William F Brinkman and Patricia E Cladis. Defects in liquid crystals. *Physics Today*, 35:48–56, 1982.

[24] F. Brochard, L. Léger, and R. B. Meyer. Freedericksz transition of a homeotropic nematic liquid crystal in rotating magnetic fields. *J. Phys. Colloques*, 36(C1):C1–209–C1–213, 1975.

[25] Miguel Camacho-Lopez, Heino Finkelmann, Peter Palffy-Muhoray, and Michael Shelley. Fast liquid-crystal elastomer swims into the dark. *Nature Materials*, 3(5):307–310, May 2004.

[26] C. Chevalier and F. Pellegrini. PT-SCOTCH: a tool for efficient parallel graph ordering. *Parallel Computing*, 34(6):318–331, 2008.

[27] Pedro A. Cruz, Murilo F. Tomé, Iain W. Stewart, and Sean McKee. Numerical solution of the Ericksen-Leslie dynamic equations for two-dimensional nematic liquid crystal flows. *Journal of Computational Physics*, 247:109 – 136, 2013.

[28] Lisandro D. Dalcin, Rodrigo R. Paz, Pablo A. Kler, and Alejandro Cosimo. Parallel distributed computing using Python. *Advances in Water Resources*, 34(9):1124–1139, 2011. New Computational Methods and Software Tools.

[29] P Dasgupta, M K Das, and B Das. Fast switching negative dielectric anisotropic multicomponent mixtures for vertically aligned liquid crystal displays. *Materials Research Express*, 2(4):045015, 2015.

[30] T. Davis and E. Gartland. Finite element analysis of the Landau-de Gennes minimization problem for liquid crystals. *SIAM Journal on Numerical Analysis*, 35(1):336–362, 1998.

[31] P. G. de Gennes and J. Prost. *The Physics of Liquid Crystals*, volume 83 of *International Series of Monographs on Physics*. Oxford Science Publication, Oxford, UK, 2nd edition, 1995.

[32] Wim H. de Jeu, editor. *Liquid Crystal Elastomers: Materials and Applications*. Advances in Polymer Science. Springer, 2012.

[33] Andrew DeBenedictis and Timothy J. Atherton. Shape minimisation problems in liquid crystals. *Liquid Crystals*, 43(13-15):2352–2362, 2016.

[34] Dietrich Demus and Lothar Richter. *Textures of liquid crystals*. Weinheim: Verlag Chemie, 1978.

[35] Amanda E. Diegel and Shawn W. Walker. A finite element method for a phase field model of nematic liquid crystal droplets. *Communications in Computational Physics*, 25:155–188, 2019.

[36] Ingo Dierking. *Textures of liquid crystals*. Wiley-VCH Verlag GmbH & Co. KGaA, 2003.

[37] Zvonimir Dogic and Seth Fraden. Ordered phases of filamentous viruses. *Current Opinion in Colloid & Interface Science*, 11(1):47–55, 2006.

[38] Hongjie Dong and Doyoon Kim. L_p solvability of divergence type parabolic and elliptic systems with partially BMO coefficients. *Calculus of Variations and Partial Differential Equations*, 40(3):357–389, Mar 2011.

[39] Jr. Eugene C. Gartland. Scalings and limits of landau-de gennes models for liquid crystals: a comment on some recent analytical papers. *Mathematical Modelling and Analysis*, 23(3):414 – 432, 2018.

[40] R. P. Feynman, R. B. Leighton, and M. Sands. *The Feynman Lectures on Physics*. Addison-Wesley Publishing Company, 1964.

[41] Avner Friedman. *Partial Differential Equations of Parabolic Type*. Dover, 2008.

[42] E. C. Gartland Jr, P. Palffy-Muhoray, and R. S. Varga. Numerical minimization of the Landau-de Gennes free energy: Defects in cylindrical capillaries. *Molecular Crystals and Liquid Crystals*, 199(1):429–452, 1991.

[43] Jun Geng. $W^{1,p}$ estimates for elliptic problems with Neumann boundary conditions in Lipschitz domains. *Advances in Mathematics*, 229(4):2427–2448, 2012.

[44] Yong Geng, Rijeesh Kizhakidathazhath, and Jan P. F. Lagerwall. Robust cholesteric liquid crystal elastomer fibres for mechanochromic textiles. *Nature Materials*, 21(12):1441–1447, Dec 2022.

[45] Mariano Giaquinta and Luca Martinazzi. *An Introductionto the Regularity Theory for Elliptic Systems, Harmonic Maps and Minimal Graphs*. Publications of the Scuola Normale Superiore. Springer.

[46] F. M. Guillén González and J. V. Gutiérrez-Santacreu. A linear mixed finite element scheme for a nematic Ericksen-Leslie liquid crystal model. *ESAIM: Mathematical Modelling and Numerical Analysis*, 47:1433–1464, 9 2013.

[47] J. W. Goodby. *Handbook of Visual Display Technology (Editors: Chen, Janglin, Cranton, Wayne, Fihn, Mark)*, chapter Introduction to Defect Textures in Liquid Crystals, pages 1290–1314. Springer, 2012.

[48] Yuedong Gu and Nicholas L. Abbott. Observation of saturn-ring defects around solid microspheres in nematic liquid crystals. *Phys. Rev. Lett.*, 85:4719–4722, Nov 2000.

[49] I. W. Hamley. Nanotechnology with soft materials. *Angewandte Chemie International Edition*, 42(15):1692–1712, 2003.

[50] Bruce Hendrickson and Robert Leland. A multilevel algorithm for partitioning graphs. In *Supercomputing '95: Proceedings of the 1995 ACM/IEEE Conference on Supercomputing (CDROM)*, page 28, New York, 1995. ACM Press.

[51] Miklós Homolya, Robert C. Kirby, and David A. Ham. Exposing and exploiting structure: optimal code generation for high-order finite element methods, 2017.

[52] Miklós Homolya, Lawrence Mitchell, Fabio Luporini, and David A. Ham. TSFC: a structure-preserving form compiler, 2017.

[53] Johan Hoogboom, Johannes A.A.W Elemans, Alan E Rowan, Theo H.M Rasing, and Roeland J.M Nolte. The development of self-assembled liquid crystal display alignment layers. *Philosophical Transactions of the Royal Society of London A: Mathematical, Physical and Engineering Sciences*, 365(1855):1553–1576, 2007.

[54] Richard James, Eero Willman, FA FernandezFernandez, and Sally E Day. Finite-element modeling of liquid-crystal hydrodynamics with a variable degree of order. *IEEE Transactions on Electron Devices*, 53(7):1575–1582, 2006.

[55] Jürgen Jost and Xianqing Li-Jost. *Calculus of Variations*. Cambridge, 1998.

[56] Samo Kralj and Apala Majumdar. Order reconstruction patterns in nematic liquid crystal wells. *Proceedings of the Royal Society of London A: Mathematical, Physical and Engineering Sciences*, 470(2169), 2014.

[57] N. V. Krylov. *Lectures on Elliptic and Parabolic Equations in Sobolev Spaces*. Graduate Studies in Mathematics. American Mathematical Society, 2008.

[58] Jan Lagerwall. Liquid crystal elastomer actuators and sensors: Glimpses of the past, the present and perhaps the future. *Programmable Materials*, 1:e9, 2023.

[59] Jan P.F. Lagerwall and Giusy Scalia. A new era for liquid crystal research: Applications of liquid crystals in soft matter nano-, bio- and microtechnology. *Current Applied Physics*, 12(6):1387 – 1412, 2012.

[60] Maxim O. Lavrentovich and Lisa Tran. Undulation instabilities in cholesteric liquid crystals induced by anchoring transitions. *Phys. Rev. Research*, 2:023128, May 2020.

[61] Gi-Dong Lee, James Anderson, and Philip J. Bos. Fast Q-tensor method for modeling liquid crystal director configurations with defects. *Applied Physics Letters*, 81(21):3951–3953, 2002.

[62] M. Lenoir. Optimal isoparametric finite elements and error estimates for domains involving curved boundaries. *SIAM Journal of Numerical Analysis*, 23(3):562–580, 1986.

[63] Fang-Hua Lin and Chun Liu. Static and dynamic theories of liquid crystals. *Journal of Partial Differential Equations*, 14(4):289–330, 2001.

[64] Fabio Luporini, David A. Ham, and Paul H. J. Kelly. An algorithm for the optimization of finite element integration loops. *ACM Transactions on Mathematical Software*, 44:3:1–3:26, 2017.

[65] Apala Majumdar. Equilibrium order parameters of nematic liquid crystals in the landau-de gennes theory. *European Journal of Applied Mathematics*, 21(2):181–203, 2010.

[66] Alina M. Martinez, Matthew K. McBride, Timothy J. White, and Christopher N. Bowman. Reconfigurable and spatially programmable chameleon skin-like material utilizing light responsive covalent adaptable cholesteric liquid crystal elastomers. *Advanced Functional Materials*, 30(35):2003150, 2020.

[67] Gianni Dal Maso, Marco Forti, Mario Miranda, Sergio A. Spagnolo, and Luigi Ambrosio, editors. *Selected Papers*. Springer Collected Works in Mathematics. Ennio De Giorgi, 2006.

[68] Hiroyuki Mori, Jr. Eugene C. Gartland, Jack R. Kelly, and Philip J. Bos. Multidimensional director modeling using the Q-tensor representation in a liquid crystal cell and its application to the π-cell with patterned electrodes. *Japanese Journal of Applied Physics*, 38(1R):135–146, 1999.

[69] Angelique Morvant, Ethan Seal, and Shawn W. Walker. A coupled Ericksen/Allen–Cahn model for liquid crystal droplets. *Computers & Mathematics with Applications*, 75(11):4048 – 4065, 2018.

[70] N. J. Mottram and C. J. P. Newton. Introduction to Q-tensor theory. *ArXiv e-prints*, September 2014.

[71] Igor Muševič, Miha Škarabot, Uroš Tkalec, Miha Ravnik, and Slobodan Žumer. Two-dimensional nematic colloidal crystals self-assembled by topological defects. *Science*, 313(5789):954–958, 2006.

[72] Ricardo H. Nochetto, Shawn W. Walker, and Wujun Zhang. A finite element

method for nematic liquid crystals with variable degree of orientation. *SIAM Journal on Numerical Analysis*, 55(3):1357–1386, 2017.

[73] Ricardo H. Nochetto, Shawn W. Walker, and Wujun Zhang. The Ericksen model of liquid crystals with colloidal and electric effects. *Journal of Computational Physics*, 352:568 – 601, 2018.

[74] Dongyeop X. Oh, Yun Jeong Cha, Hoang-Linh Nguyen, Hwa Heon Je, Yong Seok Jho, Dong Soo Hwang, and Dong Ki Yoon. Chiral nematic self-assembly of minimally surface damaged chitin nanofibrils and its load bearing functions. *Scientific Reports*, 6(1):23245, Mar 2016.

[75] G. A. Ozin, I. Manners, S. Fournier-Bidoz, and A. Arsenault. Dream nanomachines. *Advanced Materials*, 17(24):3011–3018, 2005.

[76] Alison Ramage and Eugene C. Gartland, Jr. A preconditioned nullspace method for liquid crystal director modeling. *SIAM Journal on Scientific Computing*, 35(1):B226–B247, 2013.

[77] Florian Rathgeber, David A. Ham, Lawrence Mitchell, Michael Lange, Fabio Luporini, Andrew T. T. Mcrae, Gheorghe-Teodor Bercea, Graham R. Markall, and Paul H. J. Kelly. Firedrake: Automating the finite element method by composing abstractions. *ACM Trans. Math. Softw.*, 43(3), dec 2016.

[78] Miha Ravnik and Slobodan Žumer. Landau-degennes modelling of nematic liquid crystal colloids. *Liquid Crystals*, 36(10-11):1201–1214, 2009.

[79] Andraž Rešetič, Jerneja Milavec, Blaž Zupančič, Valentina Domenici, and Boštjan Zalar. Polymer-dispersed liquid crystal elastomers. *Nature Communications*, 7:13140, 2016.

[80] N Schopohl and TJ Sluckin. Defect core structure in nematic liquid crystals. *Physical review letters*, 59(22):2582, 1987.

[81] Mathew Schwartz, Gabriele Lenzini, Yong Geng, Peter B. Rønne, Peter Y. A. Ryan, and Jan P. F. Lagerwall. Cholesteric liquid crystal shells as enabling material for information-rich design and architecture. *Advanced Materials*, 30(30):1707382, 2018.

[82] Aayush A. Shah, Heekyoung Kang, Kevin L. Kohlstedt, Kyung Hyun Ahn, Sharon C. Glotzer, Charles W. Monroe, and Michael J. Solomon. Self-assembly: Liquid crystal order in colloidal suspensions of spheroidal particles by direct current electric field assembly (small 10/2012). *Small*, 8(10):1551–1562, 2012.

[83] J. Shen and X. Yang. Numerical approximations of Allen-Cahn and Cahn-Hilliard equations. *Discrete Contin. Dyn. Syst.*, 28(4):1669 – 1691, 2010.

[84] André M. Sonnet and Epifanio Virga. *Dissipative Ordered Fluids: Theories for Liquid Crystals*. Springer, 2012.

[85] Martin Stynes and David Stynes. *Convection Diffusion Problems: An Introduction to Their Analysis and Numerical Solution*. Graduate Studies in Mathematics. AMS.

[86] Jian Sun, Huihui Wang, Ling Wang, Hui Cao, Hui Xie, Xueyao Luo, Jiumei Xiao, Hangjun Ding, Zhou Yang, and Huai Yang. Preparation and thermo-optical characteristics of a smart polymer-stabilized liquid crystal thin film based on smectic A-chiral nematic phase transition. *Smart Materials and Structures*, 23(12):125038, 2014.

[87] Thomas M. Surowiec and Shawn W. Walker. Optimal control of the landau–de gennes model of nematic liquid crystals. *SIAM Journal on Control and Optimization*, 61(4):2546–2570, 2023.

[88] Lisa Tran, Maxim O. Lavrentovich, Guillaume Durey, Alexandre Darmon, Martin F. Haase, Ningwei Li, Daeyeon Lee, Kathleen J. Stebe, Randall D. Kamien, and Teresa Lopez-Leon. Change in stripes for cholesteric shells via anchoring in moderation. *Phys. Rev. X*, 7:041029, Nov 2017.

[89] Simon Čopar, Miha Ravnik, and Slobodan Žumer. Janus nematic colloids with designable valence. *Materials*, 7(6):4272, 2014.

[90] Simon Čopar, Uroš Tkalec, Igor Muševič, and Slobodan Žumer. Knot theory realizations in nematic colloids. *Proceedings of the National Academy of Sciences*, 112(6):1675–1680, 2015.

[91] E. G. Virga. *Variational Theories for Liquid Crystals*, volume 8. Chapman and Hall, London, 1st edition, 1994.

[92] Shawn W. Walker. On The Correct Thermo-dynamic Potential for Electro-static Dielectric Energy. *arXiv 1803.08136*, mar 2018.

[93] Shawn W. Walker. A finite element method for the generalized Ericksen model of nematic liquid crystals. *ESAIM: M2AN*, 54(4):1181–1220, 2020.

[94] Noel J. Walkington. Numerical approximation of nematic liquid crystal flows governed by the Ericksen-Leslie equations. *ESAIM: Mathematical Modelling and Numerical Analysis*, 45:523–540, 5 2011.

[95] Taylor H. Ware, Michael E. McConney, Jeong Jae Wie, Vincent P. Tondiglia, and Timothy J. White. Voxelated liquid crystal elastomers. *Science*, 347(6225):982–984, 2015.

[96] S. M. Wise, C. Wang, and J. S. Lowengrub. An energy-stable and convergent finite-difference scheme for the phase field crystal equation. *SIAM J. Numer. Anal.*, 47(3):2269–2288, June 2009.

[97] Jinchao Xu, Yukun Li, Shuonan Wu, and Arthur Bousquet. On the stability and accuracy of partially and fully implicit schemes for phase field modeling. *Computer Methods in Applied Mechanics and Engineering*, 345:826 – 853, 2019.

[98] Xiaofeng Yang, M. Gregory Forest, Huiyuan Li, Chun Liu, Jie Shen, Qi Wang, and Falai Chen. Modeling and simulations of drop pinch-off from liquid crystal filaments and the leaky liquid crystal faucet immersed in viscous fluids. *Journal of Computational Physics*, 236:1 – 14, 2013.

[99] Xiaofeng Yang, M. Gregory Forest, Chun Liu, and Jie Shen. Shear cell rupture of nematic liquid crystal droplets in viscous fluids. *Journal of Non-Newtonian Fluid Mechanics*, 166(9-10):487 – 499, 2011.

[100] Jia Zhao and Qi Wang. Semi-discrete energy-stable schemes for a tensor-based hydrodynamic model of nematic liquid crystal flows. *Journal of Scientific Computing*, 68(3):1241–1266, Sep 2016.

[101] Jia Zhao, Xiaofeng Yang, Jie Shen, and Qi Wang. A decoupled energy stable scheme for a hydrodynamic phase-field model of mixtures of nematic liquid crystals and viscous fluids. *Journal of Computational Physics*, 305:539 – 556, 2016.

[102] Wei Zhu, Michael Shelley, and Peter Palffy-Muhoray. Modeling and simulation of liquid-crystal elastomers. *Phys. Rev. E*, 83:051703, May 2011.

Vita

Andrew Hicks was born and raised in Lafayette, Louisiana. He completed his B.A. in Mathematics and Economics in 2017 at Ave Maria University in Ave Maria, Florida. In 2018 he began his Ph.D. studies in Mathematics at Louisiana State University in Baton Rouge. He earned his M.S. in Mathematics from LSU in 2020 and would go on to study numerical analysis of liquid crystals under advisor Prof. Shawn Walker. He will receive his Ph.D. in May 2024.